

Alma Mater Studiorum Università di Bologna
Archivio istituzionale della ricerca

Ultraviolet-Visible Diffuse Reflectance Spectroscopy (UV-Vis DRS), a rapid and non-destructive analytical tool for the identification of Saharan dust events in Particulate Matter filters

This is the final peer-reviewed author's accepted manuscript (postprint) of the following publication:

Published Version:

Pietro Morozzi, B.B. (2021). Ultraviolet-Visible Diffuse Reflectance Spectroscopy (UV-Vis DRS), a rapid and non-destructive analytical tool for the identification of Saharan dust events in Particulate Matter filters. *ATMOSPHERIC ENVIRONMENT*, 252, 1-12 [10.1016/j.atmosenv.2021.118297].

Availability:

This version is available at: <https://hdl.handle.net/11585/813573> since: 2021-03-09

Published:

DOI: <http://doi.org/10.1016/j.atmosenv.2021.118297>

Terms of use:

Some rights reserved. The terms and conditions for the reuse of this version of the manuscript are specified in the publishing policy. For all terms of use and more information see the publisher's website.

This item was downloaded from IRIS Università di Bologna (<https://cris.unibo.it/>).
When citing, please refer to the published version.

(Article begins on next page)

This is the final peer-reviewed accepted manuscript of:

ULTRAVIOLET–VISIBLE DIFFUSE REFLECTANCE SPECTROSCOPY (UV–VIS DRS), A RAPID AND NON-DESTRUCTIVE ANALYTICAL TOOL FOR THE IDENTIFICATION OF SAHARAN DUST EVENTS IN PARTICULATE MATTER FILTERS, 2021. . ATMOSPHERIC ENVIRONMENT 252, 118297.

The final published version is available online at:
<https://doi.org/10.1016/j.atmosenv.2021.118297>.

Terms of use:

Some rights reserved. The terms and conditions for the reuse of this version of the manuscript are specified in the publishing policy. For all terms of use and more information see the publisher's website.

This item was downloaded from IRIS Università di Bologna (<https://cris.unibo.it/>)

When citing, please refer to the published version.

TITLE

Ultraviolet-Visible Diffuse Reflectance Spectroscopy (UV-Vis DRS), a rapid and non-destructive analytical tool for the identification of Saharan dust events in Particulate Matter filters

AUTHORS

Pietro Morozzi ^a

Barbara Ballarin ^b

Erika Brattich ^c

Franco Lucarelli ^d

Silvia Nava ^d

Pedro J. Gómez-Cascales ^e

Jose A. G. Orza ^e

Laura Tositti ^a

^a Department of Chemistry “G. Ciamician”, University of Bologna, Via Selmi, 2, 40126 Bologna, Italy

^b Department of Industrial Chemistry Toso Montanari, University of Bologna, Viale del Risorgimento, 4, 40136 Bologna, Italy

^c Department of Physics and Astronomy, University of Bologna, Via Irnerio, 46, 40126 Bologna, Italy

^d Department of Physics and Astronomy, University of Florence and National Institute of Nuclear Physics (INFN), Florence Section, Via Sansone, 1, 50019 Sesto Fiorentino, Italy

^e SCOLAb, Department of Applied Physics, University Miguel Hernandez de Elche, 03202 Elche, Spain

***Corresponding author:** Pietro Morozzi

e-mail address: pietro.morozzi2@unibo.it

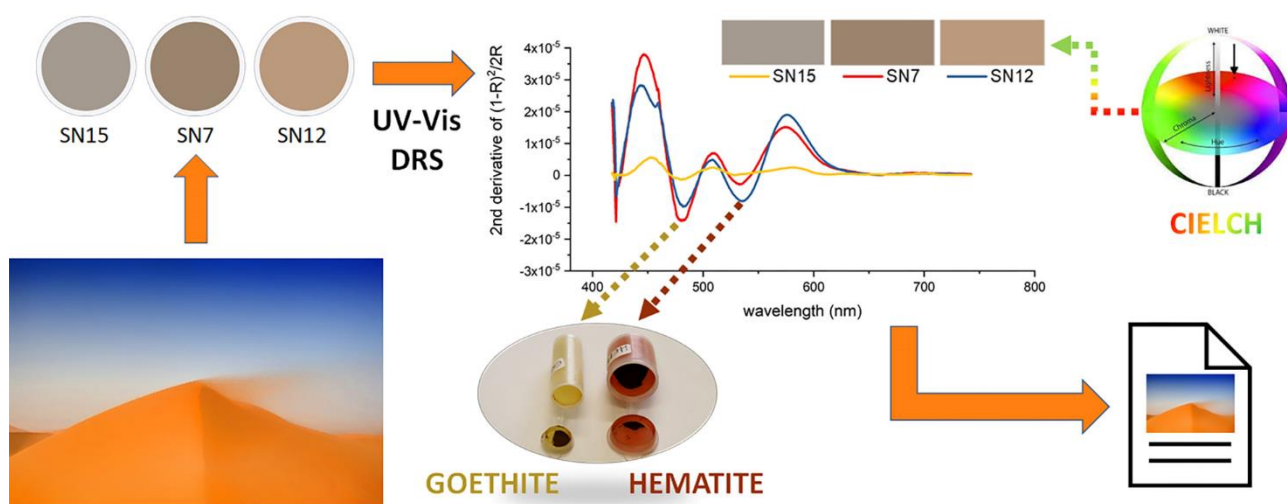
mailing address: Via Selmi 2, 40126 Bologna (ITALY)

ABSTRACT

Mineral dust represents one of the main components of particulate matter (PM) in the Mediterranean area. The rapid identification of Saharan dust events in PM samples is desirable and required for several reasons, including their role in direct effect on climate by radiative forcing as well as their adverse effects on human health.

For this purpose, the feasibility of UV-Vis Diffuse Reflectance Spectroscopy (UV-Vis DRS) is described as a rapid, inexpensive and non-destructive method of analysis of PM filters. The method developed allows to parameterize the PM filter colors and to obtain semi-quantitative data related to iron oxide minerals, mainly hematite and goethite, two of the most representative minerals of Saharan dust in the Mediterranean area. The obtained results were validated based on the correlation between the spectrophotometric data of iron oxides from the membranes with the quantitative assessment of the concentration of iron by Particle Induced X-ray Emission (PIXE). Moreover, colorimetric parameterization allows setting up a classification approach for filters with potential for a posteriori use of this data in the study of the optical behavior of aerosol particles in the air.

In this work, it is demonstrated how, as the concentration of iron mineral oxides and especially of hematite increases, the extent of redness color in PM filters grows up. Therefore, this technique can be extremely useful for a rapid, cheap and unambiguous identification of Saharan dust events in PM filters. The diagnosis of Saharan dust events was performed on PM₁₀ filters with a strong mineral dust component and demonstrated with the residence time analysis of back-trajectory ensembles, proving the reliability of this non-destructive methodology.



KEYWORDS

Saharan dust, diffuse reflectance spectroscopy, iron oxide minerals, colorimetry, chemometrics, residence time analysis

HIGHLIGHTS

- Rapid and non-destructive technique for particulate matter filter analysis
- Quick identification of filter colour
- Semi-quantitative analysis of iron oxide minerals
- Fast detection of Saharan dust events
- Determination of particular events and/or emission sources of particulate matter

1. INTRODUCTION

Mineral dust uplifted into the atmosphere by the wind in arid and semi-arid regions of North Africa are often transported across thousands of kilometers including both the northernmost European territory and/or the American continent (e.g., Middleton & Goudie, 2002). Overall the Mediterranean basin owing to proximity and average circulation patterns, is directly and widely affected by these phenomena throughout the year with events whose intensity and frequency are object of extensive research (Brattich et al., 2015a; Brattich et al., 2015b; Cabello et al., 2016; Cuevas et al., 2017; Cusack et al., 2012; Israelevich et al., 2012; Riccio et al., 2009; Tositti et al., 2014). The frequency and intensity of Saharan Dust outbreaks are presently reported as increasing due to the effect of global warming (Middleton & Goudie, 2002; Soleimani et al., 2020). These events can contribute to an increase of PM₁₀ levels above the limits allowed by the air quality regulations drawing attention on health threatens as well as on their correct management (Diapouli et al., 2017; Krasnov et al., 2014; Matassoni et al., 2011; Nava et al., 2012; Querol et al., 2019). In particular, the European Air Quality Directive 2008/50/EC establishes that PM₁₀ (i.e. PM with an aerodynamic diameter less than 10 µm) daily mean value may not exceed 50 µg/m³ more than 35 times in a year and that the PM₁₀ annual mean value may not exceed 40 µg/m³ (EU, 2008). similarly, the World Health Organization (WHO) recommends a PM₁₀ daily mean value less than 50 µg/m³ but with a considerably lower PM₁₀ annual mean value of 20 µg/m³ (WHO, 2006). The European legislation allows subtracting the contribution associated to natural episodes and therefore the quantification of the African dust contribution is

85 relevant in the air quality field (EEA, 2012). The relevance of this quantification is not limited to
86 legislation, however.

87 Saharan dust plays a significant role in the climate system by affecting the radiative balance of the
88 planet. Dust particles heavily modify the optical properties of the troposphere by the so-called direct
89 effect (e.g., Chin et al., 2009; Ginoux, 2017; IDSO, 1981; Littmann & Steinrücke, 1989; Sokolik &
90 Toon, 1999), while recent research has shown it plays also a fundamental role in cloud processing
91 and nucleation, i.e. by indirect effect (see for example Reicher et al., 2019). Furthermore, mineral
92 dust strongly influences the atmospheric reactivity through complex surface chemical reactions
93 (Usher et al., 2003). Mineral particles may also affect the oxidant capacity of the troposphere by
94 catalyzing ozone destruction, an important pollutant and reactive greenhouse gas (Bonasoni et al.,
95 2003; Dickerson et al., 1997; Prospero et al., 1995). Moreover, iron contained in Saharan dust plumes
96 can settle on oceanic surfaces and be a nutrient for marine phytoplankton, with beneficial results for
97 oligotrophic aquatic systems but potentially damaging the eutrophic ones (e.g., Bristow et al., 2010;
98 Molinaroli & Masiol, 2006). However, Saharan dust has been often associated with a coral decline in
99 the Caribbean region, suggesting that either mineral or microbiological components of Saharan dust
100 may reveal detrimental to especially fragile ecosystems (Garrison et al., 2003; Shinn et al., 2000).
101 This is in agreement with further, not negligible, implications linking Saharan dust transport with an
102 increase in the mortality rate and adverse health effects on the Mediterranean population (Karanasiou
103 et al., 2012; Querol et al., 2019; Stafoggia et al., 2016).

104 Common procedures to identify dust outbreaks use a combination of back-trajectory analysis, satellite
105 retrievals, and the output of dust prediction models. Collectively they provide a reasonable degree of
106 evidence though each of these tools has limitations: a back-trajectory travelling over North Africa is
107 not always associated to dust advection; satellite retrievals are limited by cloud coverage and transit
108 time; uncertainties in dust model estimates remain, due to incomplete representation of several
109 processes. All of this information is frequently combined with PM₁₀ levels or columnar aerosol

110 properties at the study site. These levels are compared with local threshold values or background
111 levels obtained by their own time series (Barnaba et al., 2017) or with PM₁₀ concentrations at a close
112 regional background site (EC Commission, 2011; Escudero et al., 2007). Saharan mineral dust
113 consists mainly of silicates, aluminum oxides, carbonates, gypsum, and iron oxides, with a specific
114 composition that depends on the geological material from its lifting place (e.g., Linke et al., 2006).
115 Chemical speciation analysis is largely used to characterize aerosol composition as a function of its
116 sources. Mineral dust is successfully identified with all the basic techniques devoted to elemental
117 inorganic analysis; X-ray emission techniques such as Particle Induced X-ray Emission (PIXE) and
118 X-ray fluorescence (XRF) are the most efficient and non-destructive ones since they allow a prompt
119 detection of the abundant geochemical components, without any demanding and costly chemical
120 processing in advance. Crustal elements like silicon (Si), aluminum (Al), titanium (Ti), calcium (Ca),
121 and iron (Fe) are successfully used to identify Saharan dust events, as reported by, e.g., Alastuey et
122 al., 2016; Formenti et al., 2010; Marconi et al., 2014; Nava et al., 2012; Rodríguez et al., 2020. In
123 most cases, elemental analysis is complemented by ion chromatography wherein the most informative
124 species associated with mineral dust is calcium ion (Ca²⁺) (Escudero et al., 2005; Flentje et al., 2015;
125 Putaud et al., 2004). This approach can be integrated by the detection of mineral species such as
126 quartz, feldspars, illite, smectite, kaolinite, chlorite, vermiculite, mica, calcite, gypsum, hematite and
127 goethite (Caquineau et al., 2002; Journet et al., 2014) requiring X-Ray Diffraction (XRD) (Menéndez
128 et al., 2007; Shao et al., 2007), and Scanning Electron Microscopy (SEM) (Menéndez et al., 2007;
129 Remoundaki et al., 2011). However, many of these analytical techniques are expensive, time
130 consuming, and require sophisticated instrumental facilities and highly skilled personnel.

131 In this article, a procedure based exclusively on Ultraviolet-Visible Diffuse Reflectance Spectroscopy
132 (UV-Vis DRS) (Torrent & Barrón, 2008) is proposed as a simple, cheap, efficient, rapid, and non-
133 destructive analysis of particulate samples collected on a membrane for Saharan Dust transport
134 diagnosis. This method is based on iron oxides, which account for approximately 2 to 7 % in weight

135 of the total amount of mineral dust (Alfaro et al., 2004; Formenti et al., 2008; Goudie et al., 2006) in
136 atmospheric aerosol and mainly consist of goethite (predominant, 52-78% of the total iron oxides)
137 and hematite (22-48 % of the total iron oxides) (Formenti et al., 2014; Lafon et al., 2006; Shi et al.,
138 2012). Since these minerals are important markers of mineral dust (Formenti et al., 2014; Lafon et
139 al., 2006; Shi et al., 2012), they can be used as proxies for Saharan dust events in locations
140 characterized by a low background of iron oxides from other more common sources, i.e. the Earth's
141 crust especially by soil resuspension or technogenic ones such as metal works. Hematite and goethite
142 are typically characterized by intense colors, which can impart a yellowish to red color to atmospheric
143 dust particles (Arimoto et al., 2002). The proposed methodology is characterized by: (a) color
144 parametrization and (b) iron mineral oxides semi-quantification of the analyzed PM filters, followed
145 by (c) chemometric tools. It can be integrated into routine sampling when no further speciation
146 analysis is needed. This procedure does not intend to replace the existing speciation methods, but to
147 support them in order to enhance and corroborate the identification of Saharan Dust transport
148 episodes.

149

150 **2. MATERIALS AND METHODS**

151 The Materials and Methods section is organized as follows:

152 (a) Subsection 2.1 describes the PM₁₀ samples used for the application and characterization of the
153 UV-Vis DRS methodology reported in this work;

154 (b) Subsection 2.2 describes exhaustively the method used, paying particular attention to the
155 instrumental configuration and analysis method of PM filters (subsection 2.2.1), how it is possible to
156 parameterize the colour of the analyzed filters (subsection 2.2.2) and obtain semi-quantitative data of
157 iron oxide minerals from sample reflectance spectra (subsection 2.2.3);

158 (c) Subsection 2.3 presents the validation of the proposed methodology. After checking the main
159 results of the proposed methodology (subsection 2.3.1), chemometric methods are used to identify
160 the PM filters that have been subjected to a Saharan dust transport event (subsection 2.3.2.1), and the
161 diagnosis obtained are assessed and confirmed by a residence time analysis of back-trajectory
162 ensembles (subsection 2.3.2.2).

163 **2.1 Particulate matter samples**

164 PM₁₀ samples analyzed in this work were collected at Sierra Nevada a high altitude site (37.096 N, -
165 3.387 W, 2550 m a.s.l.) in Southern Spain, within the framework of the Spanish national project
166 FRESA (Impact of dust-laden African air masses and of stratospheric air masses in the Iberian
167 Peninsula. Role of the Atlas Mountains, Ref: CGL2015-70741-R). The sampling station is located in
168 an area scarcely influenced by traffic and other anthropogenic sources, but strongly impacted by
169 Saharan dust incursion events due to its proximity to North Africa (Figure 1).

170 PM sampling was carried out using a high volume PM₁₀ sampler (CAV-A/mb, MCV S.A.) on a
171 weekly basis (168 h at 30 m³/h) using quartz filters (Ø 15 cm, Whatman QM-A quartz filters) from 8
172 June to 11 October 2016. Nineteen weekly PM₁₀ samples (labeled as SN1-SN19) were overall
173 obtained and processed along with three field blanks (labeled as B1-B3).

174 **2.2 The UV-Vis DRS methodology**

175 *2.2.1 Sample preparation and UV-Vis DRS analysis*

176 UV-Vis Diffuse Reflectance Spectroscopy is a widely used, basic spectrophotometric technique for
177 the analysis of powders and surfaces, requiring a negligible sample preparation (Torrent & Barrón,
178 2008). It is based on the surface dispersion of a fraction of the UV-Vis incident radiation on it. A UV-
179 Vis collimated light beam is directed with a certain angle onto the sample and, as a result, an ensemble
180 of optical processes leads to radiation reflection by the sample surface on the whole overlying

181 hemisphere. Generally, the radiation reflected by a sample can be considered as the sum of two
182 components: regular (or specular) and diffuse (or nondirectional) reflectance (e.g., Torrent & Barrón,
183 2008). Regular reflectance occurs when incident radiation hits an ideally smooth and planar surface
184 (i.e. without roughness) of the sample, and it is then reflected at an angle equal to the angle of
185 incidence (Fresnel law). Instead, diffuse reflectance is a combination of several optical phenomena,
186 such as multiple reflections, scattering and refraction, which disperse the radiation at all of the angles
187 of the hemisphere of origin of the incident radiation (Blitz, 1998). Diffuse reflectance is the most
188 informative component as it regards the physico-chemical properties and color of the surface (Sellitto
189 et al., 2008).

190 Diffuse reflectance spectroscopy of PM filters is conducted with an ordinary UV-Vis
191 spectrophotometer (in this work, a Perkin Elmer Lambda 35 UV-Vis Spectrophotometer was used)
192 equipped with a suitable accessory, known as integrating sphere, which allows the measurement of
193 all the reflection produced by the sample, which is diffused in the inner walls of the integrating sphere.
194 The analysis does not include any sample chemical preparation: to the scope a squared sample portion
195 of 1.8 cm x 1.8 cm is placed inside a flat sample holder, designed to position the sample for beam
196 irradiation at a 0° incidence angle, and lodged over the reflectance sample port of the integrating
197 sphere, a 50 mm diameter Labsphere RSA-PE-20 (Labsphere, United States). With the 0° sample
198 holder in place, any specular component of reflection from the sample is excluded from measurement,
199 since this component is directed out of the sphere through the transmittance sample entrance port.
200 This integrating sphere configuration is named 0°/diffuse (0°/d) and Figure 2 shows its operating
201 scheme. Square sample pieces were carefully cut by means of a square die-cutting tool with a side of
202 1.8 cm. The UV-Vis DRS analysis of the latter is non-destructive since the side containing the
203 particulate material is analyzed as it is, without any treatment and contact with the instrument. Firstly,
204 a Spectralon white standard (USRS-99-010-EPV, Labsphere, United States) was analyzed as a
205 reference and the instrumental autozero was performed. Then, one aliquot from each field blanks (B1-

206 B3) was prepared and B1 portion was used for the background correction. Subsequently, the analysis
207 of the remaining blank portions (B2 and B3) and the PM sampled filters was carried out. In particular,
208 in addition to the two blank portions, three different portions of each PM sampled filter were prepared
209 and analyzed in order to compute average values and standard deviations of each sample outcome
210 and, therefore, account for possible filter anisotropy. In this way, a total of 59 analyses were
211 completed for this work. Therefore, the percentage reflectance (% R), i.e. the ratio between the
212 intensity of the radiation reflected by the sample and the intensity of the total radiation reflected by a
213 white diffuse reflectance standard, was determined for each of the analyzed portions. In particular,
214 this parameter was measured as a function of the wavelength λ of the UV-Vis incident radiation (i.e.,
215 reflectance spectra were obtained), based on the following instrumental parameters: λ range = 780 -
216 380 nm; resolution = 0.3 nm; scan speed = 480 nm/min, smoothing = 2 nm, and slit = 2 nm.

217 2.2.2 Color parametrization

218 Sample color can be obtained by its UV-Vis reflectance spectrum. Indeed, sample color strongly
219 depends on its diffuse reflection: an object irradiated by a light source disperses part of the incident
220 radiation by diffuse reflection, which is subsequently collected by the eyes of an observer which in
221 turn act as transducers, converting the light signal into appropriate electrical impulses for the brain.
222 Ultimately, these impulses are integrated and processed by the latter, which generates the color
223 perception for the observer (Kremers et al., 2016). Therefore, color is an extremely complex and
224 subjective entity, as it is not a specific feature of the object itself but depends on many variables such
225 as the light source, the optical behavior of the object, the observer's eyes and brain, etc. Since 1931,
226 the International Commission on Illumination (CIE) has outlined guidelines to standardize color
227 perception, through the standard definition of three elements: light sources, observers, and
228 colorimetric spaces. The latter are mathematical models able to define the color of an object in a
229 rigorous manner (Ibraheem et al., 2012). One of the currently most used colorimetric space is the CIE
230 $L^*a^*b^*$ (CIELAB) (ISO-CIE 11664-4-2019), which uses three cartesian components to uniquely

231 define color sample: L^* , that indicates the CIELAB lightness in the range 0 (pure black) to 100 (pure
232 white); a^* , that indicates the CIELAB redness-greenness coordinate; and b^* , that indicates the
233 CIELAB yellowness-blueness coordinate. This colorimetric space can also be defined in polar
234 coordinates, thus obtaining the CIE $L^*C_{ab}^*h_{ab}^\circ$ space (CIELCH) (ISO-CIE 11664-4-2019), wherein:
235 L^* always indicates the CIELAB lightness; C_{ab}^* represents the CIELAB chroma, a measure of the
236 color intensity, defining how much a certain color shade is "contaminated" by gray; and h_{ab}° indicates
237 the CIELAB hue angle, whose value is expressed in degrees and describes the color tone. In
238 particular, the 0° angle represents the red color. Because of their easy interpretability, in this work
239 the mathematical definition of the colors of the analyzed portion samples was carried out employing
240 the CIELAB and CIELCH spaces, starting from the reflectance spectra obtained and using the Color
241 2.01 software (Perkin Elmer Ltd, United Kingdom). Standard Illuminant D65 was set up as a
242 representation of solar light source, according to CIE (ISO-CIE 11664-2-2020), and an observer angle
243 of 10° was set up because provide the best average spectral response in human observers (ISO-CIE
244 11664-1-2019). Average values and the standard deviations of the colorimetric parameters (L^* , a^* , b^* ,
245 C_{ab}^* , and h_{ab}°) were calculated for the blank filter (B) and the 19 samples (SN1,...SN19) starting from
246 the analyzed portions for each sample. The CIELAB average data were used for color visualization
247 through the online tool nix Color Sensor (<https://www.nixsensor.com/free-color-converter/>). In this
248 step, illuminant and reference (observer) angle have been set as D65 and 10° , respectively.

249 2.2.3 Semi-quantification of iron oxide minerals

250 Diffuse reflectance measurements are extremely useful for the individuation and quantification of the
251 most important sample pigments. Indeed, they exhibit attenuation in reflectance spectra due to their
252 light-absorption in specific UV-Vis wavelength ranges. Iron oxide minerals absorption is associated
253 with their electronic transitions within the $3d^5$ shell of Fe^{3+} ion triggered by UV-Vis radiation
254 (Scheinost et al., 1998) and, consequently, reflectance spectra can be useful for the assessment of
255 these mineral species. While past work on PM membranes was mainly based on the first derivative

256 of the UV-Vis reflectance (e.g., Arimoto et al., 2002; Shen et al., 2006), in this work we compute the
257 second derivative of the Kubelka-Munk (K-M) function spectra. This method has been widely used
258 for the assessment of iron oxides in soil samples (Barrón & Torrent, 1986; Fernandez et al., 1992;
259 Sellitto et al., 2009; Szalai et al., 2013) and less frequently for PM filters analysis (Lafon et al., 2006),
260 while the approach was used in several spectrophotometric applications for the most absorbing
261 aerosol component, i.e. soot (see for example Pandey et al., 2019; Petzold et al., 2004). The
262 calculation of the second derivative was performed using the Savitzky-Golay filter (Schafer, 2011),
263 an averaging algorithm that fits a polynomial to the data points and allows the calculation of a
264 derivative of this function. It was computed choosing a polynomial order of 4, i.e. using a fourth-
265 degree equation fit of the data points and a number of smoothing points equal to 251. Processed
266 spectra thus obtained clearly presents significant peaks due to the absorption of iron oxide minerals.
267 The semi-quantitative data of iron oxide minerals are represented by the heights of these peaks, which
268 were determined by tracing the "baselines", subtracting them from the starting spectrum, and
269 quantifying the height of the resulting peak.

The conversion of the reflectance spectra into K-M spectra was carried out using the UV WinLab
2.85 Software (Perkin Elmer Ltd, United Kingdom), while the calculation of the Savitzky-Golay
second derivative was performed by the software The Unscrambler V10.4 (Camo, Oslo, Norway),
and the quantification of peak heights was carried out using the Peak Analyzer tool of the OriginPro
2018 software (Northampton, USA).

270 **2.3 Validation of the methodology**

271 *2.3.1 Validation of UV-Vis DRS results*

272 Sample color (subsection 2.2.2) was numerically defined by means of colorimetric parameters
273 described by CIE, and semi-quantitative information about iron oxide minerals (subsection 2.2.3)
274 were achieved by a suitable mathematical treatment of reflectance spectra. In order to validate the

275 semi-quantitative data of iron oxide minerals, they were compared with elemental iron concentration
276 data ($\mu\text{g cm}^{-2}$) obtained by Proton Induced X-ray Emission (PIXE) carried out on the same PM_{10}
277 filters using a Tandetron 3 MeV accelerator located at LABEC laboratory (Laboratorio di tecniche
278 nucleari per l'Ambiente e i Beni Culturali, [https://www.ionbeamcenters.eu/RADIATE-project-](https://www.ionbeamcenters.eu/RADIATE-project-partners/inf/inf/)
279 [partners/inf/](https://www.ionbeamcenters.eu/RADIATE-project-partners/inf/inf/)) of the INFN Section of Florence (Italy) (Lucarelli et al., 2014; Lucarelli et al., 2018).
280 Since the membranes used in this work are made of quartz instead of the typical teflon (PTFE) or
281 cellulose/nuclepore, more suitable for the PIXE technique, PIXE analysis required appropriate
282 spectral processing owing to the huge interference of silicates in the filter medium itself as described
283 in detail by Calzolari et al., 2006; Chiari et al., 2018; and Lucarelli et al., 2011. In brief, PM_{10} samples
284 were irradiated with a 3.0 MeV proton beam with a 5 nA current for 60 s, with no He flow, using a
285 scanning system allowing to analyse most of the sample area and average over possible non-
286 homogeneous deposits.

Spearman correlation analysis (Akoglu, 2018) was then performed between the UV-Vis DRS outcomes (color parameters and semi-quantitative data of iron oxide minerals) with elemental iron concentration calculated by PIXE and PM_{10} obtained by gravimetry, both expressed in $\mu\text{g cm}^{-2}$ for dimensional consistency. This allowed assessing the relationship between these variables and the effectiveness of the spectrophotometric outcomes in identifying Saharan Dust events.

287 2.3.2 Diagnosis and validation of Saharan mineral dust events

288 2.3.2.1 Diagnosis based on PM filters

289 The ultimate goal of this work is to sort out quickly but safely the PM filters exposed to Saharan Dust
290 transport events from the others.

291 Therefore, Ward's cluster analysis (Ward, 1963) using squared Euclidean distance was employed for
292 the detection of two sample clusters, respectively a cluster indicating the samples subjected to Saharan
293 dust transport events and another cluster for all the other sample cases. After standardization by

294 autoscaling (van den Berg et al., 2006), the colorimetric parameters of CIELCH model (subsection
295 2.2.2) and the semi-quantitative data of iron oxide minerals (subsection 2.2.3) were used as starting
296 variables. The statistical analysis was carried out by means of the software Statistica V.10 (StatSoft
297 Inc., Tulsa, USA).

298 The two clusters obtained were subsequently compared with PM₁₀ data normalized in air sampled
299 volume ($\mu\text{g}/\text{m}^3$) in order to associate or exclude, in a binary way, the occurrence of a Saharan dust
300 incursion.

301 2.3.2.2. Back-trajectory ensembles and residence time analysis

302 A residence time analysis of back-trajectory ensembles (Lin, 2012; Lupu & Maenhaut, 2002; Stohl,
303 1998) was carried out to assess and confirm the diagnosis made by UV-Vis DRS.

304 Ensembles of back-trajectories were calculated using the NOAA Hybrid Single Particle Lagrangian
305 Integrated Trajectory (HYSPLIT_4) model (Rolph et al., 2017; Stein et al., 2015). Meteorological
306 data from the ERA-Interim reanalysis (Dee et al., 2011) was used as input for the trajectory
307 calculations with data interpolated into a 0.5-degree grid, to make use of the 0.5-degree model terrain
308 available in the Hysplit model, and 27 pressure levels from 1000 to 100 hPa. The ensemble is
309 generated by offsetting the meteorological database by one grid point in the horizontal and 0.01 sigma
310 units in the vertical, resulting in 27 back- trajectories (Draxler, 2003). 96-hour kinematic back-
311 trajectory ensembles were calculated starting 200 m over the sampling site at 00, 06, 12, and 18 UTC
312 in the period 8 June – 11 October 2016.

313 The trajectory ensembles were grouped together according to the weekly PM sampling period. After
314 that, a residence time analysis was performed by counting the number of trajectory endpoints over
315 five broad regions: Africa, America, Europe, Mediterranean Sea, and Atlantic Ocean for the
316 trajectories within each sampling period. Furthermore, two additional specific areas such as
317 Mauritania and the Atlantic Ocean at low altitude (below 800 m) were investigated. Subsequently,

the ratio between the total counts and the total number of endpoints was calculated in order to obtain percentages of residence time for each investigated area corresponding to each PM filter (Ashbaugh et al., 1985; Orza et al., 2013; Xu et al., 2006). All the trajectory calculations were performed with R (R Core Team, 2019) scripts. Further support of the occurrence of African dust events was attained with the Merged Dark Target/Deep Blue aerosol optical depth (AOD) Collection C6 product from the Moderate Resolution Imaging Spectroradiometer (MODIS) onboard the Aqua and Terra satellites.

324

3. RESULTS AND DISCUSSION

Results and discussion section is organized as follows:

- (a) Subsection 3.1 reports the colorimetric parameters and the related digitized colours for the analyzed PM filters, highlighting and discussing their differences.
- (b) Subsection 3.2 details the semi-quantitative results of iron oxide minerals, and their processing from raw reflectance spectra.
- (c) Subsection 3.3 shows the correlation between the semi-quantitative data of the iron oxide minerals, the elemental iron obtained by Proton Induced X-ray Emission (PIXE) analysis, and the colorimetric parameters.
- (d) Subsection 3.4 reveals the PM filters that have been subjected to a Saharan Dust transport event and the validation of this diagnosis by residence time analysis.

3.1 The color samples

For each portion of the PM filter analyzed, the color samples were obtained by the procedure described in subsection 2.2.2. The colorimetric parameters related to the CIELAB (L^* , a^* , b^*) and CIELCH (L^* , C_{ab}^* , h_{ab}°) models and the subsequent color obtained for the blank filter (B) and for the 19 PM samples (SN1, ...SN19) are reported in Table 1.

341 The collected PM samples present different colors (from gray to red) as a function of the dominating
 342 aerosol source during the respective sampling time interval. In order to examine how these samples
 343 differ in color, a graphical representation based on chroma (C_{ab}^*) and hue (h_{ab}°) is shown in Figure 3.
 344 First, in Figure 3 (a), it can be observed how the blank filter (B) remarkably differs from all the others
 345 (SN1, ...SN19). In fact, the B filter is characterized by a whitish color due to the absence of particulate
 346 material, while a greyish-yellowish-reddish color characterizes the sampled filters, as can be seen in
 347 the last right column of Table 1. Sampled filters in Figure 3 (b) show a defined trend: the grayest
 348 samples (like SN15) present a higher hue value and a lower chroma value than other filters while the
 349 most reddish samples (like SN12) show a higher value of chroma and a lower value of hue. Instead,
 350 the samples with intermediate values of chroma and hue (like SN7) exhibit a browner coloration than
 351 the others. This observation is in agreement with the CIELCH color definition: a lower hue value
 352 corresponds to a color tone more shifted towards red, while a higher chroma value corresponds to a
 353 more marked color intensity (compared to the gray color that occurs at chroma values close to zero).
 354 This demonstrates how the CIELCH color space adequately describes the colors of the analyzed PM
 355 filters due to their high chromaticity. In fact, the higher efficiency of the CIELCH model as compared
 356 with the CIELAB one in assessing the differences between the more chromatic colors, since C_{ab}^* and
 357 h_{ab}° allow a better identification of the more saturated colors than a and b (Schloss et al., 2018).

358 **3.2 Iron oxide minerals**

359 As previously reported in subsection 2.2.3, the calculation of the second derivative of the Kubelka-
 360 Munk function spectra was performed over the DRS spectra. This operation allows to identify
 361 decreasing peaks due to light absorption by iron oxide minerals, such as akaganéite, feroxyhyte,
 362 ferrihydrite, goethite, hematite, lepidocrocite, maghemite, and schwertmannite (Sherman & Waite,
 363 1985; Torrent & Barrón, 2002), whose characteristics are reported in Figure 4.

364 As reported by Scheinost et al., 1998, only the decreasing peak at around 535 nm is specific for a
365 single mineral (hematite), while the other peaks at 420 nm and 480 nm are shared by several other
366 iron oxides. Therefore, the semi-quantitative nature of the spectral data of iron oxide minerals can be
367 deduced for each portion of the PM filter through an appropriate processing of their UV-Vis
368 reflectance spectra. For the sake of brevity/conciseness, from now on graphical plots present the
369 results for only three characteristic filters, namely SN15, SN7, and SN12 (Figure 5). The selection of
370 the filters is not arbitrary but relies on careful considerations based on the colors determined for these
371 filters, as previously reported in subsection 3.1.

372 Figure 5 (a) reports the reflectance spectra obtained from the instrumental analysis. As can be seen,
373 these raw spectra present a characteristic baseline due to scattering of the UV-Vis radiation with tiny
374 signal decreases. Samples SN7 and SN12 in particular present two bands at around 480 nm and 535
375 nm characterized by a decrease in percentage reflectance due to absorption by iron oxides (Gonçalves
376 et al., 2012; Torrent & Barrón, 2002), a spectral feature not present in the sample SN15. Though the
377 attenuation in the reflectance signal due to iron oxide minerals can be observed, the latter does not
378 allow for accurate spectral quantification. The derivative spectroscopy has been widely used to: (a)
379 correct for baseline effects in spectra to remove non-chemical effects, (b) enhance small spectral
380 detail, and (c) resolve overlapped band (Ojeda & Rojas, 2013). Therefore, the application of
381 derivative spectroscopy can be particularly useful to enhance these iron peaks in UV-Vis reflectance
382 spectra of PM filters and, subsequently, obtain their relative semi-quantitative data. As from Figure
383 5 (b), the processed spectra present considerably more marked decreasing peaks due to iron oxides,
384 compared to the starting reflectance spectra reported in Figure 5 (a). Furthermore, the intensities of
385 the original curves can be seen in the derivatives in order of intensity, and this is necessary for
386 performing quantitative analyses. As such, three principally decreasing peaks can be identified:
387 around 420, 480 and 535 nm, respectively.

An example is reported in Figure 5 (c). The 420 nm peak was discarded as significantly affected by the instrumental spike due to the lamp shift from Vis to UV, a detail that can be noticed in Figure 5 (a) at around 380 nm. Average values and the standard deviations of the peak heights thus obtained ($h_{480\text{nm}}$ and $h_{530\text{ nm}}$) were calculated for the blank filter (B) and for the 19 samples (SN1, ...SN19) starting from the three analyzed portions for each sample, and were reported in Table 2.

3.3 Validation of UV-Vis DRS results

The similarity between the sample series of iron oxide minerals semi-quantitative data ($h_{480\text{nm}}$ and $h_{535\text{nm}}$) and elemental iron concentration (Fe) is reported in Figure 6. Figure 6 shows a comparable trend between the semi-quantitative data of iron oxide minerals and elemental iron concentration, validating the results and confirming the usefulness of the diffuse reflectance measurements in the analysis of iron mineral oxides. Table 3 reports the Spearman correlation coefficients between CIELCH parameters, iron oxide minerals semi-quantitative data, elemental iron, and PM_{10} . As can be observed, iron (Fe) is significantly linearly correlated with PM_{10} (+0.96), confirming that mineral dust is one of the main components in the analyzed samples. A high positive correlation between the height of the peaks at 480 nm and 535 nm and the concentration of iron is observed (respectively, +0.84 and +0.86) confirming the similar behavior shown in Figure 6 and proving the reliability of the semi-quantitative data on iron mineral oxides obtained from diffuse reflectance measurements. Among the two semi-quantitative data of iron oxide minerals, $h_{535\text{ nm}}$ appears as the most significantly related to filter colors (+0.85 with chroma and -0.83 with hue). This result is extremely interesting because, as previously described in subsection 3.2, this peak is specific to hematite while the other peak ($h_{480\text{nm}}$) is associated with several other iron oxides, and especially goethite. An increase in chroma and a decrease in hue leads to a higher degree in the redness of the PM filters (see subsection 3.1), which is exactly the characteristic color of hematite (Rossman, 1996). As such, the semi-quantitative data on iron oxide minerals (especially hematite) are strongly related to PM filter colors (especially the red color), and both parameters are indicative of Saharan dust transport events.

3.4 Diagnosis and validation of Saharan mineral dust events

Figure 7 reports the dendrogram obtained from Ward's clustering analysis applied to the UV-Vis DRS results (CIELCH parameters and iron oxide minerals semi-quantitative data), and where two main clusters are identified. In particular, 15 PM samples belong to cluster 1, while the other 4 PM samples belong to cluster 2. These clusters are compared with PM₁₀ data (normalized in air sampled volume, $\mu\text{g}/\text{m}^3$) in Figure 8 (a). Indeed, the association of mineral dust transport events has already been clearly related to significant increases in PM due to the considerable mass load of this component in particulate material owing to the large fraction of the coarse particles (Krasnov et al., 2014; Matassoni et al., 2011). In order to facilitate the Saharan Dust detection, the UV-Vis DRS results reported in the previous subsections are reported again in Figure 8(b) and Figure 8(c). The residence time spent by the air parcels over different areas before reaching the sampling site is also reported in Figure 9 for each PM sample.

Cluster 1 (highlighted in red) clearly identifies the Saharan dust events while cluster 2 (highlighted in green) identifies the non-Saharan dust events (Figure 8(a)). Indeed, the PM filters classified as cluster 1 are largely characterized by a higher value of PM₁₀, confirming a significant increase in PM mass load as a result of mineral dust contribution. This evidence is also supported by the color of the filters and semi-quantitative data of iron oxide minerals, (see Figures 8 (b,c)), whereas samples belonging to cluster 2 are more greyish owing to the lower concentration of iron mineral oxides, while samples belonging to cluster 1 are more brownish/reddish and with higher concentrations of iron mineral oxides. As a final not negligible data, these results agree with the outcome of the residence time analysis depicted in Figure 9 (a). The residence time analysis highlights how SN2, SN15, and SN19 samples belonging to cluster 2 are characterized by shorter residence times (less than 10%) over Africa than other PM filters (higher than 10%), suggesting uplift and rapid transport of mineral dust from the North-African desert without appreciable mixing with other aerosol sources.

Sample SN1 presents an exception being characterized by an elevated PM_{10} value and a residence time over Africa comparable to the samples belonging to the Saharan dust events cluster (cluster 1). Its assignment to the category of non-Saharan dust events, carried out only by UV-Vis DRS, is linked to its greyish color and to the low concentrations of iron oxide minerals. In order to justify this outcome, an in-depth analysis was carried out by satellite images retrieved from NASA's Earth Observing System Data and Information System (EOSDIS) (Behnke et al., 2019), shown in Figure 10. Whitish dust from the dried surface of Chott el-Jerid ephemeral lake (Figure 10(a)), was uplifted by the wind on 05/06/2016 (Figure 10(b)) and reached the receptor site on 08/06/2016 (from Figure 10(c) to Figure 10(f)), that is the first day of SN1 filter sampling period. Therefore, although the SN1 sample is significantly impacted by this Saharan dust transport event, its chemical-mineralogical composition is unusual compared to other PM samples due to the deficiency of iron oxide minerals, as evidenced by the grayish color of the examined filter.

After the classification of the Saharan dust events in the analyzed filters, some particular considerations can be drawn for some of the other samples, i.e. SN12 and SN19. SN12 is one of the PM filters more impacted by a Saharan dust events, as from its high PM_{10} concentration and its pronounced reddish color, as previously described in subsection 3.1. The latter observation may be explained by the higher value of residence time over Mauritania ($> 4\%$), as reported in Figure 9 (b), whose area is known to be an important source of reddish hematite (Journet et al., 2014; Schlueter, 2006; Waele et al., 2019). As previously assessed, sample SN19 is clearly a PM sample not affected by Saharan dust transport. This filter presents the “whitest” color amongst the samples analysed, as shown by the highest luminescence value ($L^* = 73.23$, look at Table 1) in the CIELAB/CIELCH colorimetric models. This result can be justified by a significantly long residence time over the Atlantic Ocean at low altitude ($> 5\%$), as reported in Figure 9 (c), which presumably involves a strong influence of colorless sea salt component (mainly defined by sodium chloride and magnesium chloride) in the examined filter.

4. CONCLUSIONS

In this work, the feasibility of UV-Vis Diffuse Reflectance Spectroscopy for a rapid and non-destructive diagnosis of Saharan dust events in particulate matter filters has been described, assessed, and validated. This method has been applied to particulate matter filters sampled at high altitude (2550 m a.s.l.) in an area heavily impacted by Saharan mineral dust incursion events due to its proximity to North Africa (Sierra Nevada, Spain, 37.096 N, -3.387 W).

In particular, this analytical method allowed to identify unequivocally two absorption bands corresponding to a well-defined set of iron mineral oxides contained in Saharan dust: the absorption band at about 480 nm, representative of multiple iron oxide minerals (i.e., goethite, lepidocrocite, maghemite, ferrihydrite, feroxyhyte, akaganéite, and schwertmannite), and another at about 535 nm, specific for hematite. Through appropriate processing of the obtained reflectance spectra, it has been possible to obtain semi-quantitative data for these mineral oxides. Furthermore, starting from the reflectance measurements, it has been possible to quantitatively parameterize the filter coloring as a function of PM source.

The results obtained from this technique have been validated on the basis of the elemental iron concentration obtained by Proton Induced X-ray Emission (PIXE) analysis. Besides, it has been demonstrated the relation between the concentration of hematite increases and the higher reddish color of the filters with an increase in their PM₁₀ content. Therefore, the UV-Vis DRS has been proven to be extremely useful for a fast, cheap, and unambiguous identification of Saharan mineral dust events in PM filters.

The results obtained have been finally proven on the basis of residence time analysis of back-trajectory ensembles, whose outcomes are in excellent agreement with those obtained by UV-Vis DRS, except for one PM sample with a peculiar chemical-mineralogical composition likely associated with the dried Chott el-Jerid Lake (Tunisia). Furthermore, some other samples have been explored

481 by associating the color and the semi-quantitative data of iron oxide minerals with their particular PM
482 sources.

483 In conclusion, the UV-Vis DRS technique can be reliably adopted for Saharan dust events under
484 certain conditions:

- 485 - The prevailing emission source of PM filters must be mineral dust. Indeed, a complex mixture
486 of sources can alter the color and mineralogical composition of the sampled filters, making
487 the identification of Saharan dust events extremely complicated; however, it is important to
488 highlight that in this work weekly PM₁₀ samples have been used, certainly affected by a
489 complex mixture of emission sources and, despite this, reasonable outcomes have been
490 achieved.
- 491 - Iron oxide minerals prove as efficient but also practically utilizable markers of Saharan
492 mineral dust. This is valid in most cases even though, in this work, it has been highlighted
493 that this spectroscopic technique is not capable to identify whitish sand events, characterized
494 by low concentrations of iron oxide minerals.

495

496 **ACKNOWLEDGEMENTS**

497 This work has been carried out under the Spanish project FRESA (Impact of dust-laden African air
498 masses and of stratospheric air masses in the Iberian Peninsula. Role of the Atlas Mountains, Ref:
499 CGL2015-70741-R). Firstly, Lucas Alados-Arboledas (IISTA-CEAMA) is gratefully acknowledged
500 for making possible the field campaign at the sampling site. A Heartfelt thanks to Sara Arcozzi, for
501 her technical assistance on the Perkin Elmer Lambda 35 UV-Vis Spectrophotometer, and Christian
502 Cingolani, Josep Mestres Sanna, and Adrià Simon Ortiz for the assistance in the experimental activity
503 during their thesis work. Finally, the authors acknowledge the NOAA Air Resources Laboratory
504 (ARL) for the provision of the HYSPLIT transport and dispersion model and/or READY website

505 (<https://www.ready.noaa.gov>) used in this publication and the European Centre for Medium-range
506 Weather Forecast (ECMWF) for making available the ERA-Interim database.

507

508 **REFERENCES**

509 Akoglu, H. (2018). User's guide to correlation coefficients. Turkish Journal of Emergency Medicine,
510 18. <https://doi.org/10.1016/j.tjem.2018.08.001>

511 Alastuey, A., Querol, X., Aas, W., Lucarelli, F., Pérez, N., Moreno, T., ... Yttri, K. E. (2016).
512 Geochemistry of PM₁₀ over Europe during the EMEP intensive measurement periods in summer
513 2012 and winter 2013. Atmos. Chem. Phys., 16(10), 6107–6129. [https://doi.org/10.5194/acp-16-](https://doi.org/10.5194/acp-16-6107-2016)
514 6107-2016

515 Alfaro, S., Lafon, S., Rajot, J., Formenti, P., Gaudichet, A., & Maillé, M. (2004). Iron oxides and
516 light absorption by pure desert dust: An experimental study. Journal of Geophysical Research
517 (Atmospheres), 109, 8208. <https://doi.org/10.1029/2003JD004374>

518 Arimoto, R., Balsam, W., & Schloesslin, C. (2002). Visible spectroscopy of aerosol particles
519 collected on filters: Iron-oxide minerals. Atmospheric Environment, 36, 89–96.
520 [https://doi.org/10.1016/S1352-2310\(01\)00465-4](https://doi.org/10.1016/S1352-2310(01)00465-4)

521 Ashbaugh, L. L., Malm, W. C., & Sadeh, W. Z. (1985). A residence time probability analysis of sulfur
522 concentrations at grand Canyon National Park. Atmospheric Environment (1967), 19(8), 1263–1270.
523 [https://doi.org/https://doi.org/10.1016/0004-6981\(85\)90256-2](https://doi.org/https://doi.org/10.1016/0004-6981(85)90256-2)

524 Barnaba, F., Bolignano, A., di Liberto, L., Morelli, M., Lucarelli, F., Nava, S., ... Gobbi, G. P. (2017).
525 Desert dust contribution to PM₁₀ loads in Italy: Methods and recommendations addressing the
526 relevant European Commission Guidelines in support to the Air Quality Directive 2008/50.
527 Atmospheric Environment, 161. <https://doi.org/10.1016/j.atmosenv.2017.04.038>

528 Barrón, V., & Torrent, J. (1986). Use of the Kubelka—Munk theory to study the influence of iron
529 oxides on soil colour. *Journal of Soil Science*, 37(4), 499–510.

530 Behnke, J., Mitchell, A., & Ramapriyan, H. (2019). NASA’s Earth Observing Data and Information
531 System – Near-Term Challenges. *Data Science Journal*, 18. <https://doi.org/10.5334/dsj-2019-040>

532 Blitz, J. P. (1998). Diffuse reflectance spectroscopy. *Modern Techniques in Applied Molecular*
533 *Spectroscopy*, 14, 185.

534 Bonasoni, P., Cristofanelli, P., Sandro, F., Gobbi, G. P., van Dingenen, R., Tositti, L., & Balkanski,
535 Y. (2003). Ozone and aerosol correlation during Saharan dust transport episodes at Mt. Cimone.

536 Brattich, E, Hernández-Ceballos, M. A., Cinelli, G., & Tositti, L. (2015a). Analysis of ²¹⁰Pb peak
537 values at Mt. Cimone (1998–2011). *Atmospheric Environment*, 112, 136–147.
538 [https://doi.org/https://doi.org/10.1016/j.atmosenv.2015.04.020](https://doi.org/10.1016/j.atmosenv.2015.04.020)

539 Brattich, Erika, Riccio, A., Tositti, L., Cristofanelli, P., & Bonasoni, P. (2015b). An outstanding
540 Saharan dust event at Mt. Cimone (2165 m asl, Italy) in March 2004. *Atmospheric Environment*, 113,
541 223–235.

542 Bristow, C. S., Hudson-Edwards, K. A., & Chappell, A. (2010). Fertilizing the Amazon and equatorial
543 Atlantic with West African dust. *Geophysical Research Letters*, 37(14).

544 Cabello, M., G. Orza, J., Dueñas, C., Liger, E., Gordo, E., & Cañete, S. (2016). Back-trajectory
545 analysis of African dust outbreaks at a coastal city in southern Spain: Selection of starting heights
546 and assessment of African and concurrent Mediterranean contributions. *Atmospheric Environment*,
547 140. <https://doi.org/10.1016/j.atmosenv.2016.05.047>

548 Calzolari, G., Chiari, M., García Orellana, I., Lucarelli, F., Migliori, A., Nava, S., & Taccetti, F.
549 (2006). The new external beam facility for environmental studies at the Tandatron accelerator of

550 LABEC. Nuclear Instruments and Methods in Physics Research Section B: Beam Interactions with
 551 Materials and Atoms, 249(1), 928–931. <https://doi.org/https://doi.org/10.1016/j.nimb.2006.03.193>

552 Caquineau, S., Gaudichet, A., Gomes, L., & Legrand, M. (2002). Mineralogy of Saharan dust
 553 transported over northwestern tropical Atlantic Ocean in relation to source regions. Journal of
 554 Geophysical Research: Atmospheres, 107(D15), AAC 4-1-AAC 4-12.
 555 <https://doi.org/10.1029/2000JD000247>

556 Chiari, M., Yubero, E., Calzolari, G., Lucarelli, F., Crespo, J., Galindo, N., ... Nava, S. (2018).
 557 Comparison of PIXE and XRF analysis of airborne particulate matter samples collected on Teflon
 558 and quartz fibre filters. Nuclear Instruments and Methods in Physics Research Section B: Beam
 559 Interactions with Materials and Atoms, 417, 128–132.
 560 <https://doi.org/https://doi.org/10.1016/j.nimb.2017.07.031>

561 Chin, M., Diehl, T., Dubovik, O., Eck, T., Holben, B., Sinyuk, A., & Streets, D. (2009). Light
 562 absorption by pollution, dust, and biomass burning aerosols: A global model study and evaluation
 563 with AERONET measurements. Annales Geophysicae, 27. [https://doi.org/10.5194/angeo-27-3439-](https://doi.org/10.5194/angeo-27-3439-2009)
 564 2009

565 Cuevas, E., Gómez-Peláez, A. J., Rodríguez, S., Terradellas, E., Basart, S., García, R. D., ... Alonso-
 566 Pérez, S. (2017). The pulsating nature of large-scale Saharan dust transport as a result of interplays
 567 between mid-latitude Rossby waves and the North African Dipole Intensity. Atmospheric
 568 Environment, 167, 586–602.

569 Cusack, M., Alastuey, A., Pérez, N., Pey, J., & Querol, X. (2012). Trends of particulate matter (PM_{2.5}) and chemical composition at a regional background site in the Western Mediterranean over the last
 570 nine years (2002–2010). Atmos. Chem. Phys, 12(18), 8341–8357.

572 Dee, D., P. de, Uppala, Simmons, Berrisford, Poli, P., ... Vitart, F. (2011). The ERA-Interim
573 reanalysis: Configuration and performance of the data assimilation system. Quarterly Journal of the
574 Royal Meteorological Society, 137, 553–597. <https://doi.org/10.1002/qj.828>

575 Diapouli, E., Manousakas, M. I., Vratolis, S., Vasilatou, V., Pateraki, S., Bairachtari, K. A., ...
576 Eleftheriadis, K. (2017). AIRUSE-LIFE +: estimation of natural source contributions to urban
577 ambient air PM₁₀ and PM_{2.5} concentrations in southern Europe – implications to compliance with
578 limit values. Atmos. Chem. Phys., 17(5), 3673–3685. <https://doi.org/10.5194/acp-17-3673-2017>

579 Dickerson, R., Kondragunta, S., Stenchikov, G., Civerolo, K., Doddridge, B., & Holben, B. (1997).
580 The impact of aerosol on solar UV radiation and photochemical smog. Science (New York, N.Y.),
581 278, 827–830. <https://doi.org/10.1126/science.278.5339.827>

582 Draxler, R. R. (2003). Evaluation of an Ensemble Dispersion Calculation. Journal of Applied
583 Meteorology, 42(2), 308–317. [https://doi.org/10.1175/1520-](https://doi.org/10.1175/1520-0450(2003)042<0308:EOAEDC>2.0.CO;2)
584 [0450\(2003\)042<0308:EOAEDC>2.0.CO;2](https://doi.org/10.1175/1520-0450(2003)042<0308:EOAEDC>2.0.CO;2)

585 EC Commission (2011). Staff Working Paper establishing guidelines for determination of
586 contributions from the re-suspension of particulates following winter sanding or salting of roads under
587 the Directive 2008/50/EC on ambient air quality and cleaner air for Europe. European Commission,
588 SEC. 2011; 2011:207.
589 http://ec.europa.eu/environment/air/quality/legislation/pdf/sec_2011_0207.pdf

590 EEA, Technical report No 10/2012 (2012). Particulate matter from natural sources and related
591 reporting under the EU Air Quality Directive in 2008 and 2009. ISBN: 978-92-9213-325-2.
592 <https://www.eea.europa.eu/publications/particulate-matter-from-natural-sources>

593 Escudero, M., Castillo, S., Querol, X., Avila, A., Alarcón, M., Viana, M. M., ... Rodríguez, S. (2005).
 594 Wet and dry African dust episodes over eastern Spain. *Journal of Geophysical Research:*
 595 *Atmospheres*, 110(D18). <https://doi.org/10.1029/2004JD004731>

596 Escudero, M., Querol, X., Pey, J., Alastuey, A., Pérez, N., Ferreira, F., ... Cuevas, E. (2007). A
 597 methodology for the quantification of the net African dust load in air quality monitoring networks.
 598 *Atmospheric Environment*, 41(26), 5516–5524.
 599 <https://doi.org/10.1016/j.atmosenv.2007.04.047>

600 EU (2008). Directive 2008/50/EC of the European Parliament and of the Council of 21 May 2008 on
 601 ambient air quality and cleaner air for Europe. *Official Journal of the European Union*.

602 Fernandez, R. N., & Schulze, D. G. (1992). Munsell colors of soils simulated by mixtures of goethite
 603 and hematite with kaolinite. *Zeitschrift Für Pflanzenernährung Und Bodenkunde*, 155(5), 473–478.

604 Flentje, H., Briel, B., Beck, C., Collaud Coen, M., Fricke, M., Cyrys, J., ... Thomas, W. (2015).
 605 Identification and monitoring of Saharan dust: An inventory representative for south Germany since
 606 1997. *Atmospheric Environment*, 109, 87–96.
 607 <https://doi.org/10.1016/j.atmosenv.2015.02.023>

608 Formenti, P., Caquineau, S., Chevaillier, S., Klaver, A., Desboeufs, K., Rajot, J., ... Briois, V. (2014).
 609 Dominance of goethite over hematite in iron oxides of mineral dust from Western Africa: quantitative
 610 partitioning by X-ray Absorption Spectroscopy. *Journal of Geophysical Research: Atmospheres*, 119.
 611 <https://doi.org/10.1002/2014JD021668>

612 Formenti, P., Nava, S., Prati, P., Chevaillier, S., Klaver, A., Lafon, S., ... Chiari, M. (2010). Self-
 613 attenuation artifacts and correction factors of light element measurements by X-ray analysis:
 614 Implication for mineral dust composition studies. *Journal of Geophysical Research*, 115.
 615 <https://doi.org/10.1029/2009JD012701>

616 Formenti, P., Rajot, J., Desboeufs, K., Caquineau, S., Chevallier, S., Nava, S., ... Highwood, E.
617 (2008). Regional variability of the composition of mineral dust from western Africa: Results from
618 the AMMA SOP0/DABEX and DODO field campaigns. *J. Geophys. Res.*, 113.
619 <https://doi.org/10.1029/2008JD009903>

620 Garrison, V. H., Shinn, E. A., Foreman, W. T., Griffin, D. W., Holmes, C. W., Kellogg, C. A., ...
621 Smith, G. W. (2003). African and Asian Dust: From Desert Soils to Coral Reefs. *BioScience*, 53(5),
622 469–480. [https://doi.org/10.1641/0006-3568\(2003\)053\[0469:AAADFD\]2.0.CO;2](https://doi.org/10.1641/0006-3568(2003)053[0469:AAADFD]2.0.CO;2)

623 Ginoux, P. (2017). Warming or cooling dust? *Nature Geoscience*, 10(4), 246–248.
624 <https://doi.org/10.1038/ngeo2923>

625 Gonçalves, Í. G., Petter, C. O., & Machado, J. L. (2012). Quantification of hematite and goethite
626 concentrations in kaolin using diffuse reflectance spectroscopy: a new approach to Kubelka-Munk
627 theory. *Clays and Clay Minerals*, 60(5), 473–483.

628 Goudie, A., & Middleton, N. (2006). Desert Dust in the Global System. *Desert Dust in the Global*
629 *System*, 1–287. <https://doi.org/10.1007/3-540-32355-4>

630 Ibraheem, N., Hasan, M., Khan, R. Z., & Mishra, P. (2012). Understanding Color Models: A Review.
631 *ARNP Journal of Science and Technology*, 2.

632 IDSO, S. (1981). Climatic change: The role of atmospheric dust. *Special Paper of the Geological*
633 *Society of America*, 186, 207–215. <https://doi.org/10.1130/SPE186-p207>

634 ISO-CIE 11664-1-2019. Colorimetry - CIE standard colorimetric observers. Standard, International
635 Organization for Standardization, Geneva, CH.

636 ISO-CIE 11664-2-2020. Colorimetry - Part 2: CIE standard illuminants. Standard, International
637 Organization for Standardization, Geneva, CH.

638 ISO-CIE 11664-4-2019. Colorimetry - Part 4: CIE 1976 L*a*b* colour space. Standard, International
639 Organization for Standardization, Geneva, CH.

640 Israelevich, P., Ganor, E., Alpert, P., Kishcha, P., & Stupp, A. (2012). Predominant transport paths
641 of Saharan dust over the Mediterranean Sea to Europe. *Journal of Geophysical Research:*
642 *Atmospheres*, 117(D2).

643 Journet, E., Balkanski, Y., & Harrison, S. (2014). A new data set of soil mineralogy for dust-cycle
644 modeling. *ATMOSPHERIC CHEMISTRY AND PHYSICS*, 14, 3801–3816.
645 <https://doi.org/10.5194/acp-14-3801-2014>

646 Karanasiou, A., Moreno, N., Moreno, T., Viana, M., de Leeuw, F., & Querol, X. (2012). Health
647 effects from Sahara dust episodes in Europe: Literature review and research gaps. *Environment*
648 *International*, 47, 107–114. <https://doi.org/10.1016/j.envint.2012.06.012>

649 Krasnov, H., Katra, I., Koutrakis, P., & Friger, M. (2014). Contribution of dust storms to PM10 levels
650 in an urban arid environment. *Journal of the Air & Waste Management Association* (1995), 64, 89–
651 94. <https://doi.org/10.1080/10962247.2013.841599>

652 Kremers, J., Baraas, R., & Marshall, N. (2016). Human Color Vision. [https://doi.org/10.1007/978-3-](https://doi.org/10.1007/978-3-319-44978-4)
653 [319-44978-4](https://doi.org/10.1007/978-3-319-44978-4)

654 Lafon, S., Sokolik, I., Rajot, J., Caquineau, S., & Gaudichet, A. (2006). Characterization of iron
655 oxides in mineral dust aerosols: Implications for light absorption. *Journal of Geophysical Research*,
656 111. <https://doi.org/10.1029/2005JD007016>

657 Lin, J. (2012). Lagrangian Modeling of the Atmosphere: An Introduction. In *Geophysical Monograph*
658 *Series* (Vol. 200). <https://doi.org/10.1029/2012GM001376>

659 Linke, C., Möhler, O., Veres, A., Mohácsi, Á., Bozóki, Z., Szabó, G., & Schnaiter, M. (2006). Optical
 660 properties and mineralogical composition of different Saharan mineral dust samples: a laboratory
 661 study. *Atmos. Chem. Phys.*, 6(11), 3315–3323. <https://doi.org/10.5194/acp-6-3315-2006>
 662 Littmann, T., & Steinrücke, J. (1989). Atmospheric boundary conditions of recent Saharan dust influx
 663 into Central Europe. *GeoJournal*, 18, 399–406. <https://doi.org/10.1007/BF00772694>
 664 Lucarelli, F., Calzolari, G., Chiari, M., Giannoni, M., Mochi, D., Nava, S., & Carraresi, L. (2014). The
 665 upgraded external-beam PIXE/PIGE set-up at LABEC for very fast measurements on aerosol
 666 samples. *Nuclear Instruments and Methods in Physics Research Section B: Beam Interactions with*
 667 *Materials and Atoms*, 318, 55–59. <https://doi.org/https://doi.org/10.1016/j.nimb.2013.05.099>
 668 Lucarelli, F., Calzolari, G., Chiari, M., Nava, S., & Carraresi, L. (2018). Study of atmospheric aerosols
 669 by IBA techniques: The LABEC experience. *Nuclear Instruments and Methods in Physics Research*
 670 *Section B: Beam Interactions with Materials and Atoms*, 417, 121–127.
 671 <https://doi.org/https://doi.org/10.1016/j.nimb.2017.07.034>
 672 Lucarelli, F., Nava, S., Calzolari, G., Chiari, M., Udisti, R., & Marino, F. (2011). Is PIXE still a useful
 673 technique for the analysis of atmospheric aerosols? The LABEC experience. *X-Ray Spectrometry*,
 674 40, 162–167. <https://doi.org/10.1002/xrs.1312>
 675 Lupu, A., & Maenhaut, W. (2002). Application and comparison of two statistical trajectory
 676 techniques for identification of source regions of atmospheric aerosol species. *Atmospheric*
 677 *Environment*, 36(36), 5607–5618. [https://doi.org/https://doi.org/10.1016/S1352-2310\(02\)00697-0](https://doi.org/https://doi.org/10.1016/S1352-2310(02)00697-0)
 678 Marconi, M., Sferlazzo, D. M., Becagli, S., Bommarito, C., Calzolari, G., Chiari, M., ... Udisti, R.
 679 (2014). Saharan dust aerosol over the central Mediterranean Sea: PM10 chemical composition and
 680 concentration versus optical columnar measurements. *Atmos. Chem. Phys.*, 14(4), 2039–2054.
 681 <https://doi.org/10.5194/acp-14-2039-2014>

682 Matassoni, L., Pratesi, G., Centioli, D., Cadoni, F., Lucarelli, F., Nava, S., & Malesani, P. (2011).
683 Saharan dust contribution to PM₁₀, PM_{2.5} and PM₁ in urban and suburban areas of Rome: A
684 comparison between single-particle SEM-EDS analysis and whole-sample PIXE analysis. *Journal of*
685 *Environmental Monitoring* : JEM, 13, 732–742. <https://doi.org/10.1039/c0em00535e>

686 Menéndez, I., Díaz-Hernández, J. L., Mangas, J., Alonso, I., & Sánchez-Soto, P. J. (2007). Airborne
687 dust accumulation and soil development in the North-East sector of Gran Canaria (Canary Islands,
688 Spain). *Journal of Arid Environments*, 71(1), 57–81.
689 <https://doi.org/https://doi.org/10.1016/j.jaridenv.2007.03.011>

690 Middleton, N., & Goudie, A. (2002). Saharan dust: Sources and trajectories. *Transactions of the*
691 *Institute of British Geographers*, 26, 165–181. <https://doi.org/10.1111/1475-5661.00013>

692 Molinaroli, E., & Masiol, M. (2006). Particolato atmosferico e ambiente mediterraneo. Il caso delle
693 polveri sahariane.

694 Nava, S., Becagli, S., Calzolari, G., Chiari, M., Lucarelli, F., Prati, P., ... Vecchi, R. (2012). Saharan
695 dust impact in central Italy: An overview on three years elemental data records. *Atmospheric*
696 *Environment*, 60, 444–452. <https://doi.org/https://doi.org/10.1016/j.atmosenv.2012.06.064>

697 WHO (2006). WHO Air quality guidelines for particulate matter, ozone, nitrogen dioxide and sulfur
698 dioxide : global update 2005 : summary of risk assessment (p. WHO/SDE/PHE/OEH/06.02). p.
699 WHO/SDE/PHE/OEH/06.02. World Health Organization.

700 Ojeda, C. B., & Rojas, F. S. (2013). Recent applications in derivative ultraviolet/visible absorption
701 spectrophotometry: 2009–2011: a review. *Microchemical Journal*, 106, 1–16.

702 Orza, J. A. G., Cabello, M., Galiano, V., Vermeulen, A. T., & Stein, A. F. (2013). The Association
703 Between the North Atlantic Oscillation and the Interannual Variability of the Tropospheric Transport

704 Pathways in Western Europe. In *Lagrangian Modeling of the Atmosphere* (pp. 127–142).
705 <https://doi.org/10.1029/2012GM001315>

706 Pandey, A., Shetty, N. J., & Chakrabarty, R. K. (2019). Aerosol light absorption from optical
707 measurements of PTFE membrane filter samples: sensitivity analysis of optical depth measures.
708 *Atmos. Meas. Tech.*, 12(2), 1365–1373. <https://doi.org/10.5194/amt-12-1365-2019>

709 Petzold, A., & Schönlinner, M. (2004). Multi-angle absorption photometry—a new method for the
710 measurement of aerosol light absorption and atmospheric black carbon. *Journal of Aerosol Science*,
711 35(4), 421–441. <https://doi.org/https://doi.org/10.1016/j.jaerosci.2003.09.005>

712 Prospero, J., Schmitt, R., Cuevas, E., Savoie, D., Graustein, W., Turekian, K., ... II, H. (1995).
713 Temporal variability of summer-time ozone and aerosols in the free troposphere over the eastern
714 North Atlantic. *Geophysical Research Letters*, 22, 2925–2928. <https://doi.org/10.1029/95GL02791>

715 Putaud, J.-P., van Dingenen, R., Dell’Acqua, A., Raes, F., Matta, E., Decesari, S., ... Fuzzi, S. (2004).
716 Size-segregated aerosol mass closure and chemical composition in Monte Cimone (I) during
717 MINATROC.

718 Querol, X., Tobías, A., Pérez, N., Karanasiou, A., Amato, F., Stafoggia, M., ... Alastuey, A. (2019).
719 Monitoring the impact of desert dust outbreaks for air quality for health studies. *Environment*
720 *International*, 130, 104867. <https://doi.org/https://doi.org/10.1016/j.envint.2019.05.061>

721 R Core Team (2019). R: A language and environment for statistical computing. R Foundation for
722 Statistical Computing, Vienna, Austria. URL <https://www.R-project.org/>.

723 Reicher, N., Budke, C., Eickhoff, L., Raveh-Rubin, S., Kaplan-Ashiri, I., Koop, T., & Rudich, Y.
724 (2019). Size-dependent ice nucleation by airborne particles during dust events in the eastern
725 Mediterranean. *Atmos. Chem. Phys.*, 19(17), 11143–11158. [https://doi.org/10.5194/acp-19-11143-](https://doi.org/10.5194/acp-19-11143-2019)
726 2019

727 Remoundaki, E., Bourliva, A., Kokkalis, P., Mamouri, R. E., Papayannis, A., Grigoratos, T., ...
 728 Tsezos, M. (2011). PM10 composition during an intense Saharan dust transport event over Athens
 729 (Greece). *Science of The Total Environment*, 409(20), 4361–4372.
 730 <https://doi.org/https://doi.org/10.1016/j.scitotenv.2011.06.026>

731 Riccio, A., Chianese, E., Tositti, L., Baldacci, D., & Sandrini, S. (2009). Modeling the transport of
 732 Saharan dust toward the Mediterranean region: an important issue for its ecological implications.
 733 *Ecological Questions*, 11, 65–72.

734 Rodríguez, S., Calzolari, G., Chiari, M., Nava, S., García, M. I., López-Solano, J., ... Querol, X.
 735 (2020). Rapid changes of dust geochemistry in the Saharan Air Layer linked to sources and
 736 meteorology. *Atmospheric Environment*, 223, 117186.
 737 <https://doi.org/https://doi.org/10.1016/j.atmosenv.2019.117186>

738 Rolph, G., Stein, A., & Stunder, B. (2017). Real-time Environmental Applications and Display
 739 sYstem: READY. *Environmental Modelling & Software*, 95, 210–228.
 740 <https://doi.org/https://doi.org/10.1016/j.envsoft.2017.06.025>

741 Rossman, G. (1996). Why hematite is red: Correlation of optical absorption intensities and magnetic
 742 moments of Fe³⁺ minerals. 5, 23–27.

743 Schafer, R. (2011). What Is a Savitzky-Golay Filter? [Lecture Notes]. *IEEE Signal Processing*
 744 *Magazine* - *IEEE SIGNAL PROCESS MAG*, 28, 111–117.
 745 <https://doi.org/10.1109/MSP.2011.941097>

746 Scheinost, A., Chavernas, A., Barrón, V., & Torrent, J. (1998). Use and limitations of second-
 747 derivative diffuse reflectance spectroscopy in the visible to near-infrared range to identify and
 748 quantify Fe oxides in soils. *Clays and Clay Minerals*, 46, 528–536.
 749 <https://doi.org/10.1346/CCMN.1998.0460506>

750 Schloss, K. B., Lessard, L., Racey, C., & Hurlbert, A. C. (2018). Modeling color preference using
 751 color space metrics. *Vision Research*, 151, 99–116.
 752 <https://doi.org/https://doi.org/10.1016/j.visres.2017.07.001>

753 Schlueter, T. (2006). Geological Atlas of Africa: With Notes on Stratigraphy, Tectonics, Economic
 754 Geology, Geohazards and Geosites of Each Country. <https://doi.org/10.1007/3-540-29145-8>

755 Sellitto, V., Barrón, V., Palumbo, G., Salzano, R., & Colombo, C. (2008). Uso della spettrometria di
 756 riflettanza diffusa (DRS) e bi-direzionale (BRF) per lo studio dei suoli vulcanici europei.

757 Sellitto, V. M., Fernandes, R. B. A., Barrón, V., & Colombo, C. (2009). Comparing two different
 758 spectroscopic techniques for the characterization of soil iron oxides: Diffuse versus bi-directional
 759 reflectance. *Geoderma*, 149(1–2), 2–9.

760 Shao, L., Li, W., Yang, S., Shi, Z., & Lü, S. (2007). Mineralogical characteristics of airborne particles
 761 collected in Beijing during a severe Asian dust storm period in spring 2002. *Science in China Series*
 762 *D: Earth Sciences*, 50(6), 953–959. <https://doi.org/10.1007/s11430-007-0035-7>

763 Shen, Z. X., Cao, J. J., Zhang, X. Y., Arimoto, R., Ji, J. F., Balsam, W. L., ... Li, X. X. (2006).
 764 Spectroscopic analysis of iron-oxide minerals in aerosol particles from northern China. *Science of*
 765 *the Total Environment*, 367(2–3), 899–907.

766 Sherman, D. M., & Waite, T. D. (1985). Electronic spectra of Fe³⁺ oxides and oxide hydroxides in
 767 the near IR to near UV. *American Mineralogist*, 70(11–12), 1262–1269. Retrieved from
 768 <http://pubs.er.usgs.gov/publication/70012311>

769 Shi, Z., Krom, M. D., Jickells, T. D., Bonneville, S., Carslaw, K. S., Mihalopoulos, N., ... Benning,
 770 L. G. (2012). Impacts on iron solubility in the mineral dust by processes in the source region and the
 771 atmosphere: A review. *Aeolian Research*, 5, 21–42.
 772 <https://doi.org/https://doi.org/10.1016/j.aeolia.2012.03.001>

773 Shinn, E. A., Smith, G. W., Prospero, J. M., Betzer, P., Hayes, M. L., Garrison, V., & Barber, R. T.
774 (2000). African dust and the demise of Caribbean Coral Reefs. *Geophysical Research Letters*, 27(19),
775 3029–3032. <https://doi.org/10.1029/2000GL011599>

776 Sokolik, I. N., & Toon, O. B. (1999). Incorporation of mineralogical composition into models of the
777 radiative properties of mineral aerosol from UV to IR wavelengths. *Journal of Geophysical Research:*
778 *Atmospheres*, 104(D8), 9423–9444. <https://doi.org/10.1029/1998JD200048>

779 Soleimani, Z., Teymouri, P., Darvishi Boloorani, A., Mesdaghinia, A., Middleton, N., & Griffin, D.
780 W. (2020). An overview of bioaerosol load and health impacts associated with dust storms: A focus
781 on the Middle East. *Atmospheric Environment*, 223, 117187.
782 <https://doi.org/https://doi.org/10.1016/j.atmosenv.2019.117187>

783 Stafoggia, M., Zauli-Sajani, S., Pey, J., Samoli, E., Alessandrini, E., Basagaña, X., ... Díaz, J. (2016).
784 Desert dust outbreaks in Southern Europe: contribution to daily PM10 concentrations and short-term
785 associations with mortality and hospital admissions. *Environmental Health Perspectives*, 124(4),
786 413–419.

787 Stein, A. F., Draxler, R. R., Rolph, G. D., Stunder, B. J. B., Cohen, M. D., & Ngan, F. (2015).
788 NOAA's HYSPLIT Atmospheric Transport and Dispersion Modeling System. *Bulletin of the*
789 *American Meteorological Society*, 96(12), 2059–2077. <https://doi.org/10.1175/BAMS-D-14-00110.1>

790 Stohl, A. (1998). Computation, accuracy and applications of trajectories—A review and bibliography.
791 *Atmospheric Environment*, 32(6), 947–966. [https://doi.org/https://doi.org/10.1016/S1352-](https://doi.org/https://doi.org/10.1016/S1352-2310(97)00457-3)
792 [2310\(97\)00457-3](https://doi.org/https://doi.org/10.1016/S1352-2310(97)00457-3)

793 Szalai, Z., Kiss, K., Jakab, G., Sipos, P., Belucz, B., & Németh, T. (2013). The use of UV-VIS-NIR
794 reflectance spectroscopy to identify iron minerals. *Astronomische Nachrichten*, 334(9), 940–943.

795 Torrent, J., & Barrón, V. (2002). Diffuse Reflectance Spectroscopy of Iron Oxides. *Encyclopedia of*
796 *Surface and Colloid Science*, 1.

797 Torrent, J., & Barrón, V. (2008). *Methods of Soil Analysis. Part 5. Mineralogical Methods*, Chapter
798 13 *Diffuse Reflectance Spectroscopy*, SSSA Book Series, No. 5. USA, 367–385.

799 Tositti, L., Brattich, E., Cinelli, G., & Baldacci, D. (2014). 12 years of ⁷Be and ²¹⁰Pb in Mt. Cimone,
800 and their correlation with meteorological parameters. *Atmospheric Environment*, 87, 108–122.
801 [https://doi.org/https://doi.org/10.1016/j.atmosenv.2014.01.014](https://doi.org/10.1016/j.atmosenv.2014.01.014)

802 Usher, C. R., Michel, A. E., & Grassian, V. H. (2003). Reactions on mineral dust. *Chemical Reviews*,
803 103(12), 4883–4940.

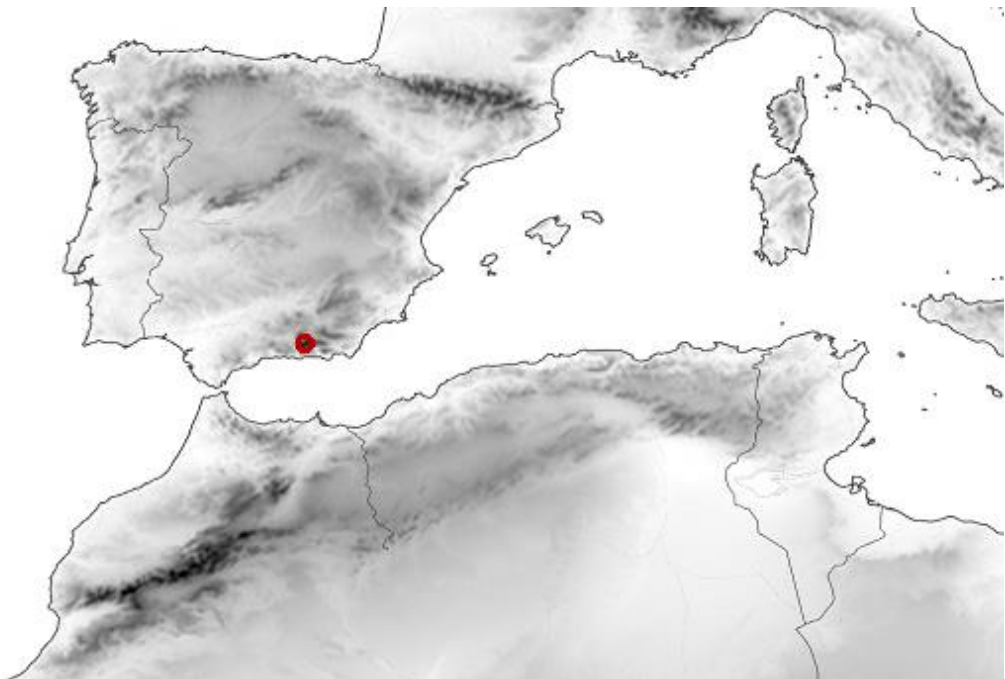
804 van den Berg, R., Hoefsloot, H., Westerhuis, J., Smilde, A., & van der Werf, M. (2006). Van den
805 Berg RA, Hoefsloot HCJ, Westerhuis JA, Smilde AK, Van der Werf MJ.. Centering, scaling, and
806 transformations: improving the biological information content of metabolomics data. *BMC Genomics*
807 7: 142-157. *BMC Genomics*, 7, 142. <https://doi.org/10.1186/1471-2164-7-142>

808 Waele, B. de, Aitken, A., Mourik, M. van, Laab Laab, K. O., Elhacen Ould Med Yeslem, M., &
809 Mohamedou, T. (2019). From a Mining Mindset to Regional Discovery: A Case Study for Hematite
810 Iron Ore Exploration in Mauritania. *ASEG Extended Abstracts*, 2019(1), 1–3.
811 <https://doi.org/10.1080/22020586.2019.12073145>

812 Ward, J. H. (1963). Hierarchical groupings to optimize an objective function. *J. Am. Stat. Assoc.*,
813 234–244.

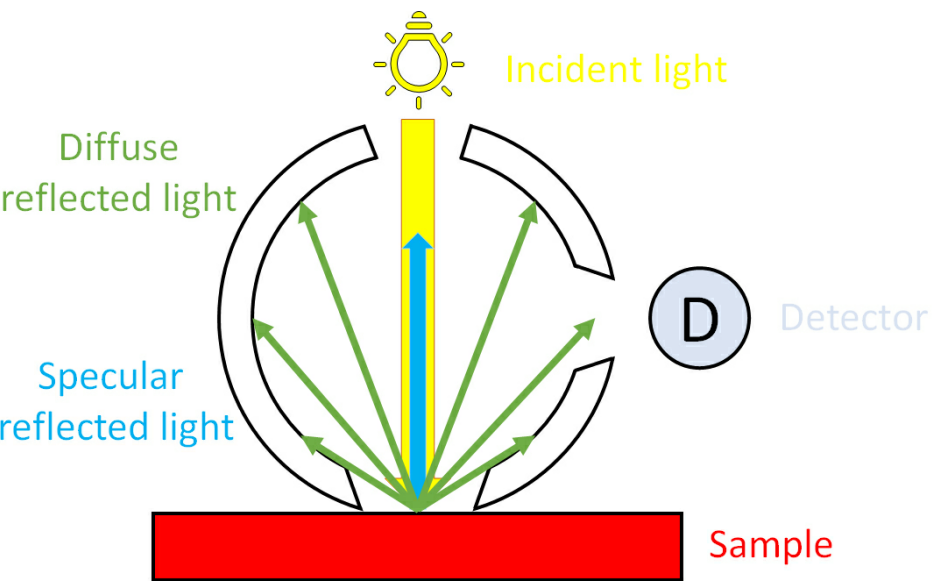
814 Xu, J., DuBois, D., Pitchford, M., Green, M., & Etyemezian, V. (2006). Attribution of sulfate aerosols
815 in Federal Class I areas of the western United States based on trajectory regression analysis.
816 *Atmospheric Environment*, 40(19), 3433–3447.
817 [https://doi.org/https://doi.org/10.1016/j.atmosenv.2006.02.009](https://doi.org/10.1016/j.atmosenv.2006.02.009)

818 **FIGURES:**



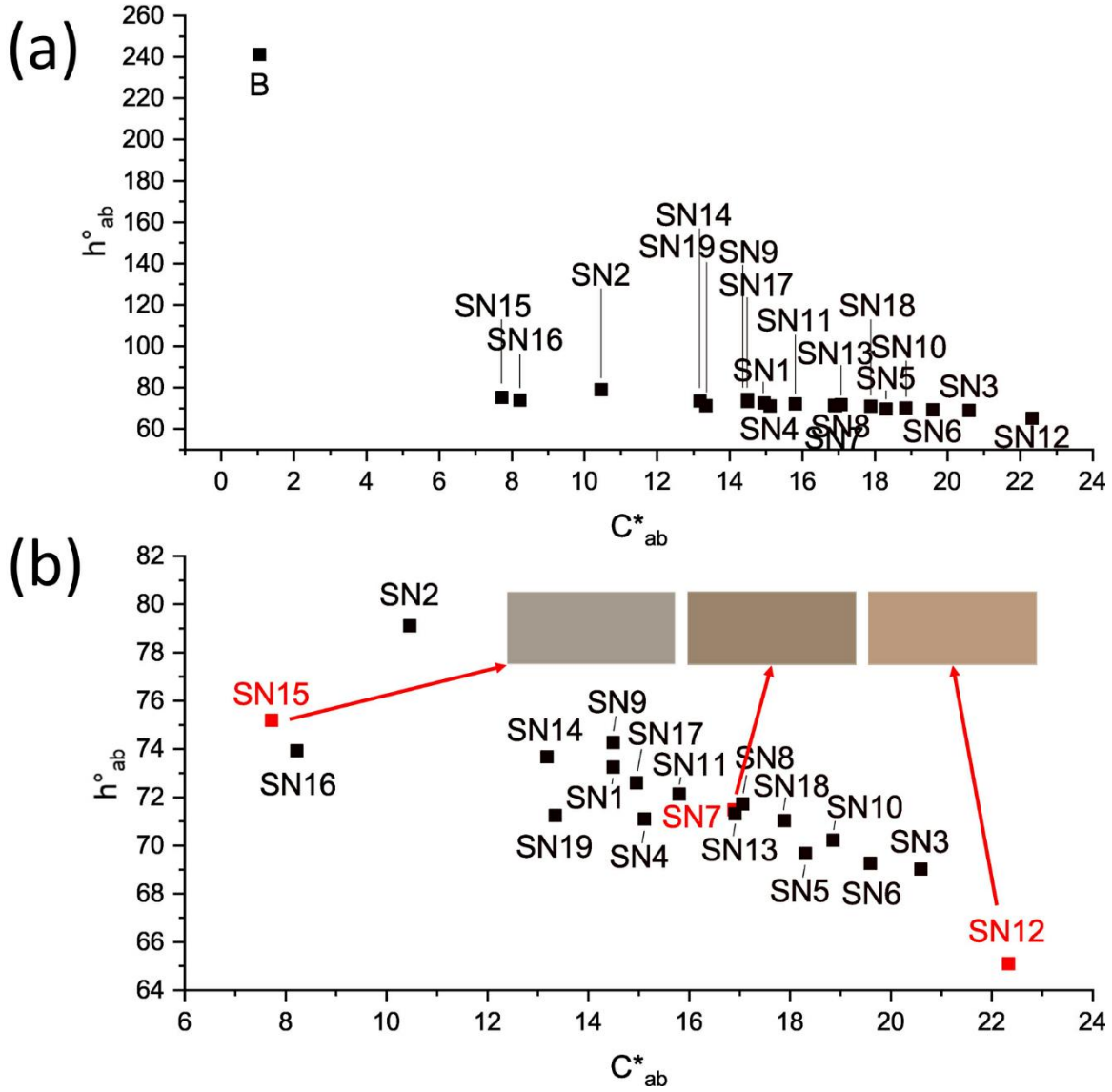
819

820 Figure 1. Map and location of Sierra Nevada sampling station.



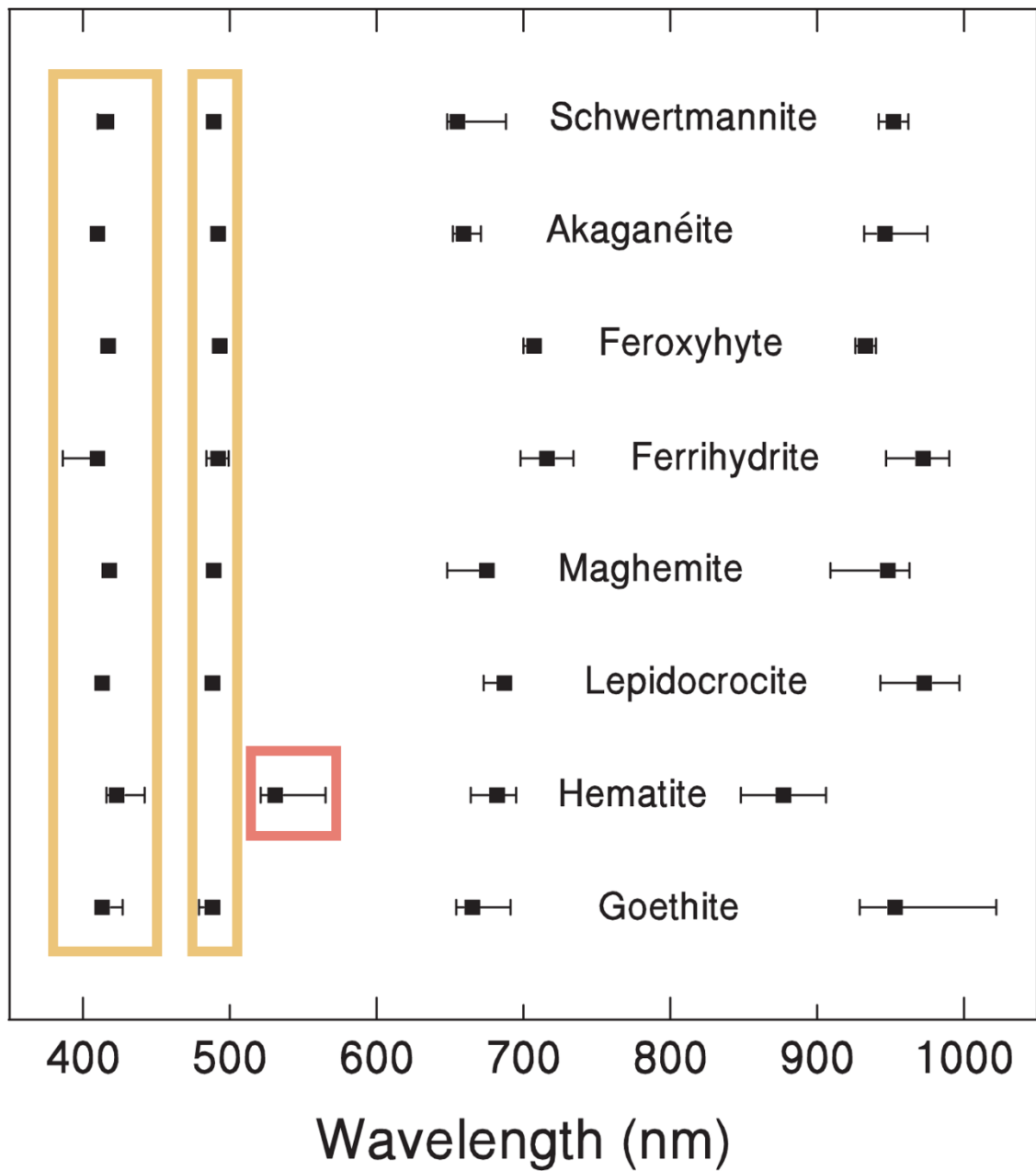
821

822 Figure 2. Scheme of the integrating sphere, 0°/d geometry. The UV-Vis incident light hits the sample
823 perpendicularly. Any specular component of reflection from the sample is excluded from
824 measurement since this component is directed out of the sphere through the transmittance sample
825 entrance port and, therefore, the detector only measures the diffuse reflectance component.



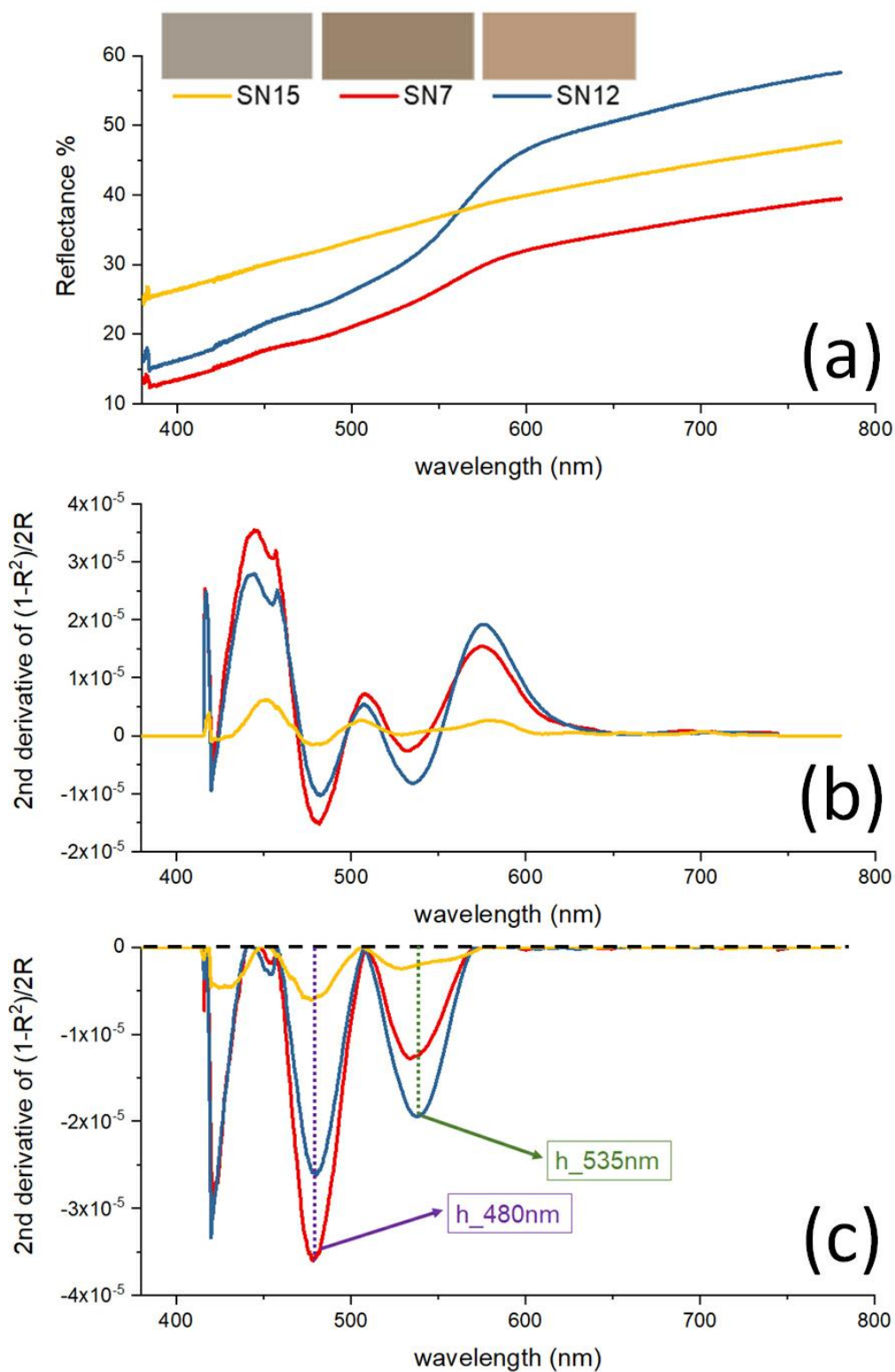
826

827 Figure 3. (a) Graphic representation of blank filter (B) and sampled filters (SN1, ...SN19) based on
 828 chroma (C_{ab}^*) and hue (h_{ab}°). (b) Zoomed plot on sampled filters. The colors of three specific samples
 829 (SN15, SN7, SN12) are shown.



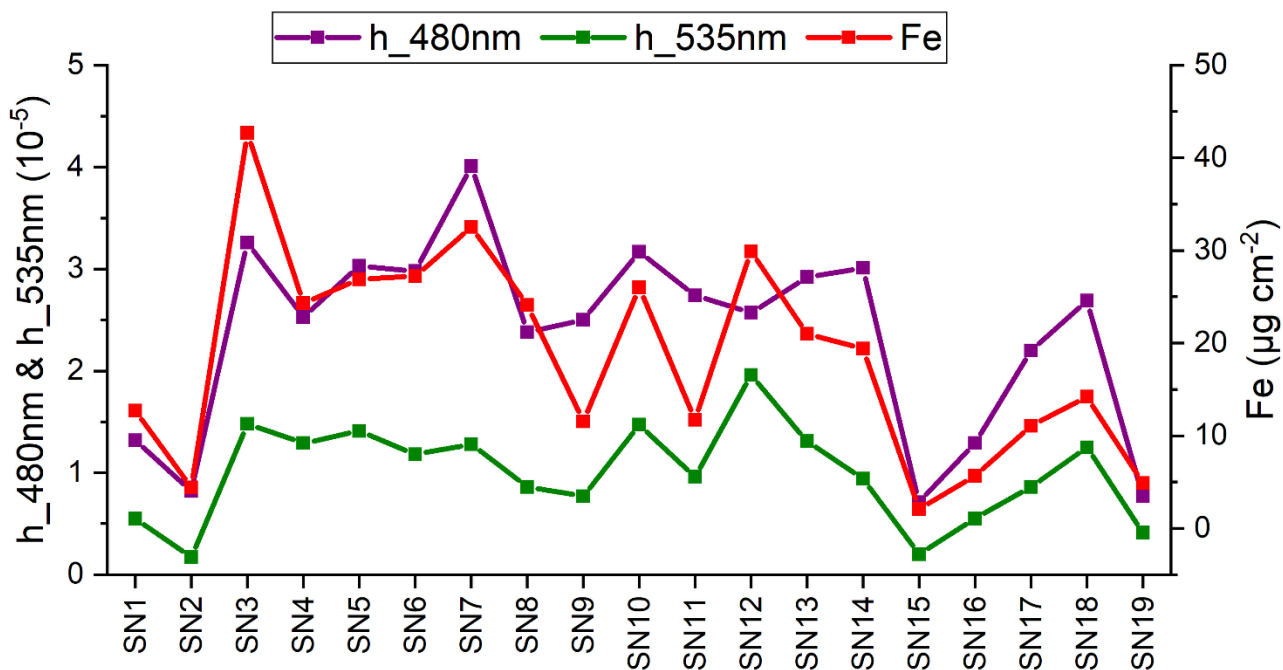
830

831 Figure 4. Median and range of the UV-Vis absorption bands of some iron oxide minerals in the second
 832 derivative of K-M function spectra, adapted from Torrent & Barrón, 2008. It can be seen that below
 833 600 nm, there are three absorption bands at around 420, 480, and 535 nm.



834

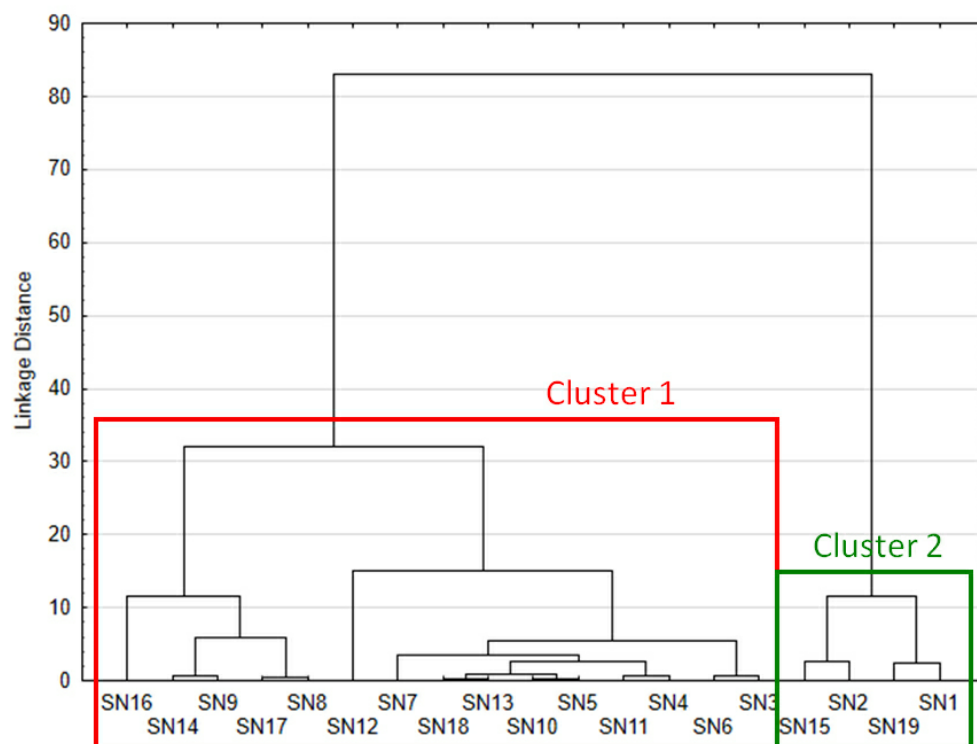
835 Figure 5. Reflectance spectra (a), Savitzky-Golay second derivative of Kubelka-Munk (K-M)
 836 function spectra (b), and baseline subtraction and quantification of relevant peak heights (c) for SN15
 837 (grayish filter), SN7 (brownish filter), and SN12 (reddish filter).



838

839 Figure 6. Sample series of h_480nm (semi-quantitative data of several iron oxide minerals, mainly

840 goethite), h_535nm (semi-quantitative data of hematite), and elemental iron concentration (Fe).

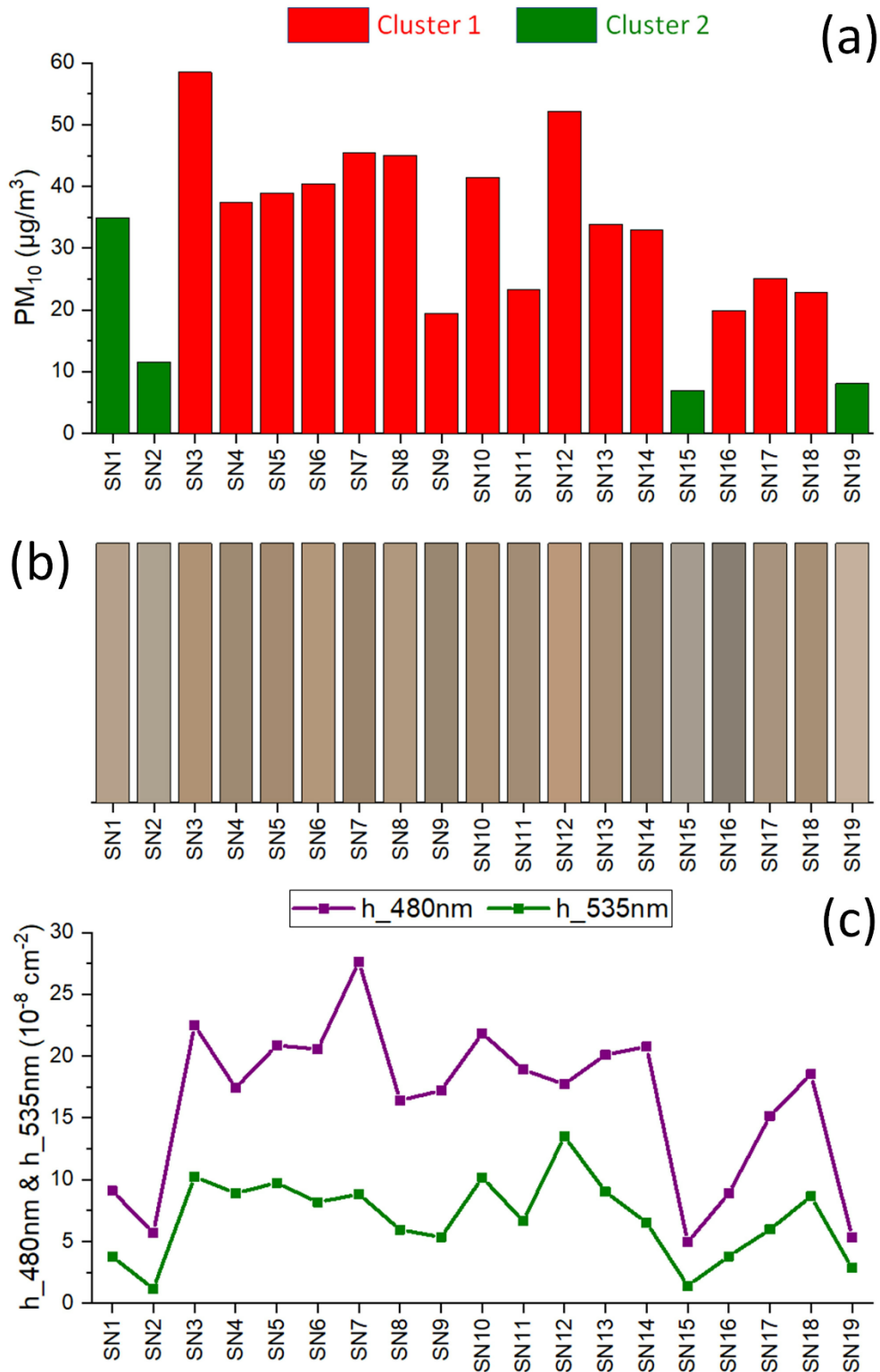


841

842 Figure 7. Dendrogram of Ward's hierarchical clustering method starting from CIELCH parameters

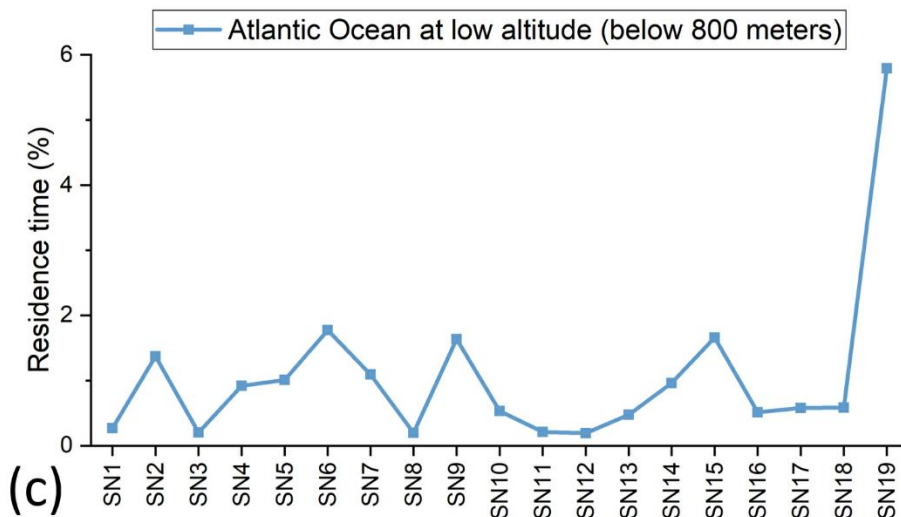
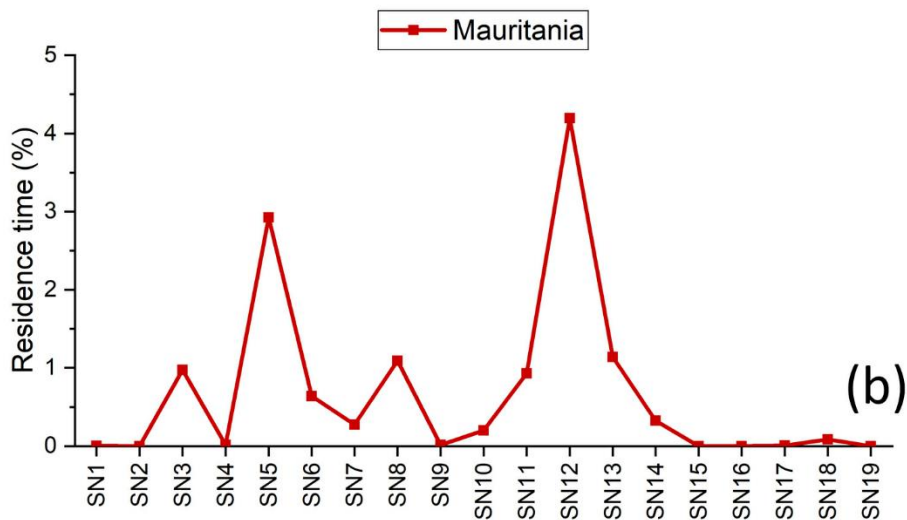
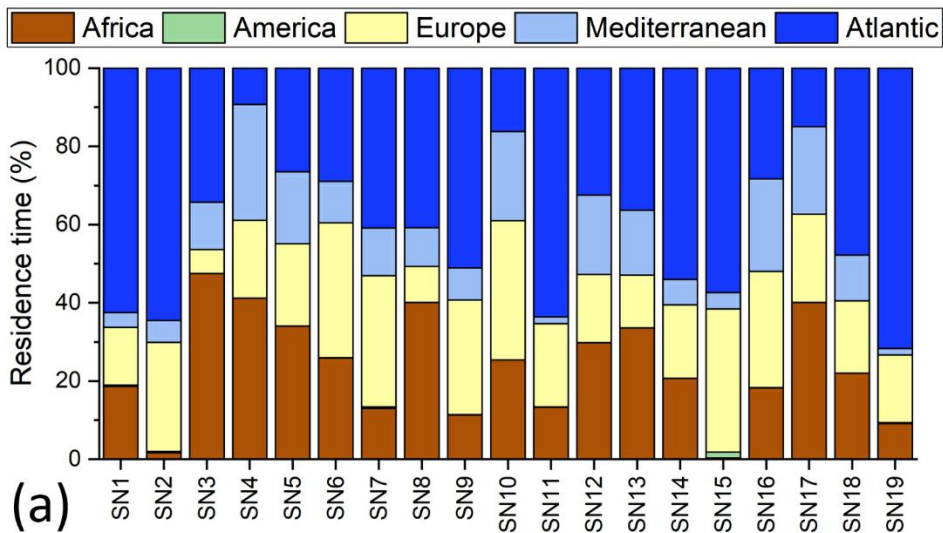
843 and semi-quantitative data of iron oxide minerals. The clustering solution with two clusters is

844 highlighted by squares.



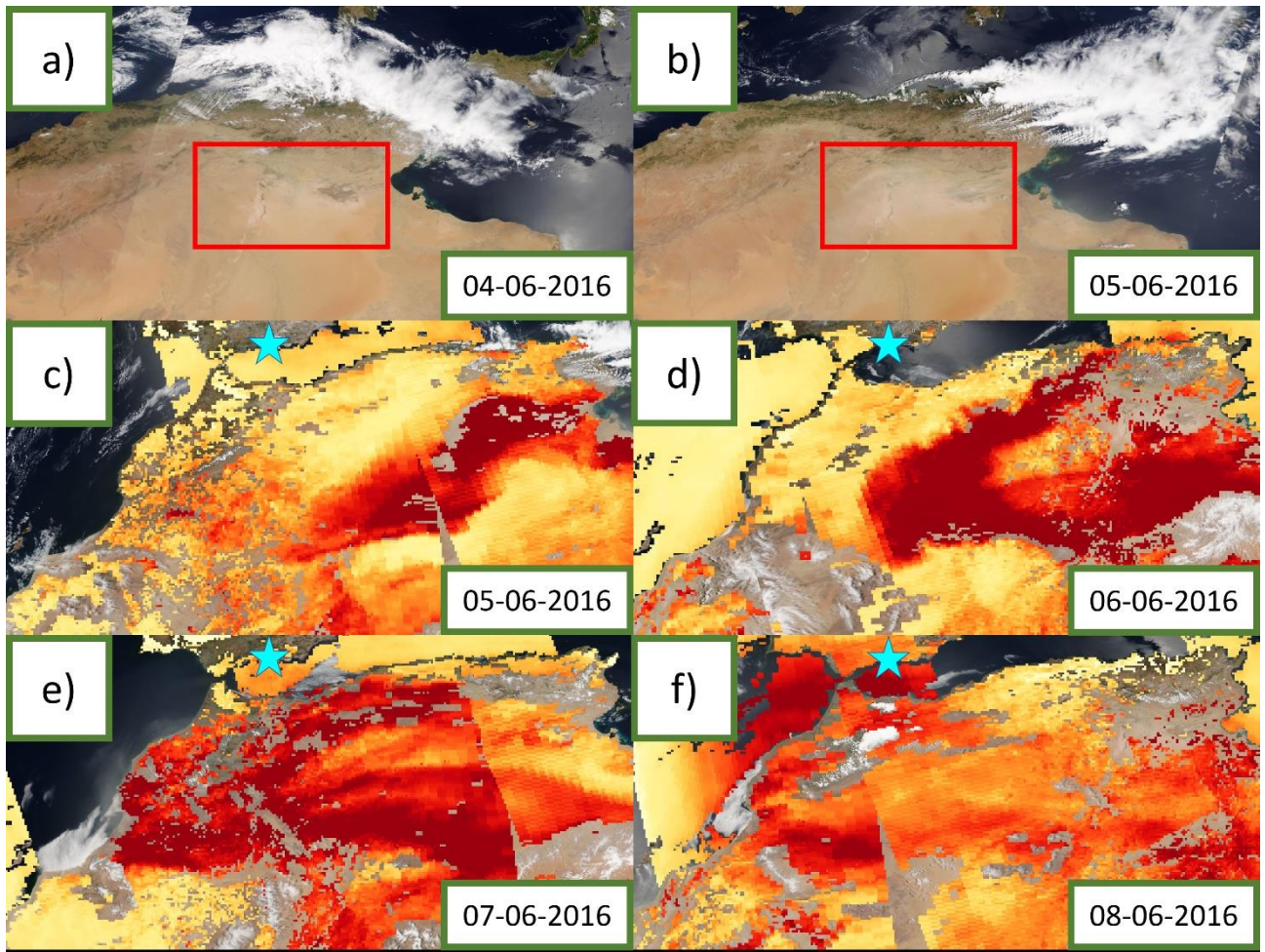
845

846 Figure 8. (a) Sample series of PM_{10} data ($\mu g/m^3$) with the association of PM filters to the respective
847 clusters (cluster 1 and cluster 2). (b) Display of PM filters colors, look at subsection 3.1. (c) Sample
848 series of h_{480nm} (semi-quantitative data of several iron oxide minerals) and h_{535nm} (hematite),
849 look at subsection 3.2.



850

851 Figure 9. (a) Stacked bar chart of the percentage residence time over each examined region and PM
 852 filter; Sample series of residence time over Mauritania (b) and the Atlantic Ocean, below 800 meters
 853 (c).



854

855 Figure 10. Corrected reflectance (True Color) Terra/MODIS snapshots for 4 June 2016 (a) and 5 June
856 2016 (b); Merged DT/DB Aerosol Optical Depth (Land and Ocean) Aqua/MODIS snapshots from 5
857 June 2016 (c) to 8 June 2016 (f). Higher AOD values are indicated by a more reddish color and allow
858 following the dust plume transport. The red square in a) and b) highlights the Chott el-Jerid Lake
859 (Tunisia) while the light blue star in c), d), e), and f) indicates the PM sampling station in Sierra
860 Nevada (37.096 N, -3.387 W, 2550 m a.s.l.). Images have been retrieved from the NASA EOSDIS,
861 worldview tool at <https://worldview.earthdata.nasa.gov>.

862

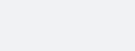



















863

864

865

866 **TABLES:**

867 Table 1. Average values and standard deviations (numbers in brackets) of the colorimetric
868 parameters for the analyzed samples. The colors obtained from the conversion to RGB color model
869 by the online tool nix Color Sensor (<https://www.nixsensor.com/free-color-converter/>) are displayed
870 in the last column of this table.

Sample	L*	a*	b*	C _{ab} *	h _{ab} °	Color
B	95.46 (0.11)	-0.51 (0.05)	-0.92 (0.13)	1.05 (0.14)	241.15 (0.81)	
SN1	67.49 (2.68)	4.14 (1.19)	13.89 (4.42)	14.49 (4.57)	73.26 (0.64)	
SN2	66.85 (3.60)	1.99 (0.43)	10.27 (1.08)	10.46 (1.13)	79.11 (1.53)	
SN3	62.63 (3.07)	7.37 (0.56)	19.23 (1.36)	20.59 (1.47)	69.03 (0.11)	
SN4	58.53 (2.46)	4.86 (1.55)	14.31 (4.99)	15.11 (5.22)	71.10 (0.71)	
SN5	59.27 (2.79)	6.33 (0.09)	17.16 (1.64)	18.30 (1.56)	69.67 (1.66)	
SN6	64.43 (2.91)	6.84 (0.46)	18.35 (3.35)	19.59 (3.28)	69.27 (2.52)	
SN7	56.77 (2.12)	5.36 (0.39)	16.02 (1.22)	16.89 (1.28)	71.48 (0.14)	
SN8	64.35 (1.41)	5.37 (1.63)	16.20 (4.63)	17.06 (4.90)	71.72 (0.38)	
SN9	57.51 (3.59)	3.94 (0.51)	13.94 (1.26)	14.49 (1.35)	74.27 (0.70)	
SN10	61.20 (3.26)	6.41 (1.31)	17.72 (2.97)	18.85 (3.23)	70.22 (0.79)	
SN11	59.83 (3.63)	4.86 (0.81)	15.04 (2.11)	15.80 (2.25)	72.13 (0.89)	
SN12	65.59 (0.76)	9.41 (1.52)	20.24 (2.92)	22.33 (3.28)	65.11 (0.65)	
SN13	60.28 (3.57)	5.43 (0.80)	16.02 (1.76)	16.91 (1.93)	71.31 (0.78)	
SN14	56.44 (1.09)	3.72 (0.95)	12.65 (2.98)	13.18 (3.13)	73.68 (0.49)	
SN15	64.91 (2.89)	1.94 (0.32)	7.47 (1.86)	7.72 (1.88)	75.19 (1.56)	
SN16	53.75 (2.55)	2.25 (0.27)	7.90 (1.52)	8.22 (1.53)	73.93 (1.58)	
SN17	62.68 (2.65)	4.46 (0.53)	14.27 (2.03)	14.95 (2.09)	72.60 (0.90)	
SN18	61.01 (2.99)	5.80 (0.09)	16.91 (1.04)	17.88 (1.00)	71.04 (0.98)	
SN19	73.23 (2.41)	4.20 (0.56)	12.63 (2.16)	13.34 (1.97)	71.24 (4.53)	

878 Table 2. Average values and standard deviations (numbers in brackets) of the semi-quantitative data
879 of mixed iron oxide minerals (h_480nm) and hematite (h_535 nm).

Sample	h_480nm (10 ⁻⁵)	h_530nm (10 ⁻⁵)
B	0.025 (0.009)	0.011 (0.005)
SN1	1.32 (0.37)	0.55 (0.08)
SN2	0.83 (0.16)	0.17 (0.04)
SN3	3.27 (0.71)	1.49 (0.20)
SN4	2.53 (1.20)	1.29 (0.17)
SN5	3.03 (0.03)	1.42 (0.06)
SN6	2.99 (0.27)	1.19 (0.19)
SN7	4.01 (0.38)	1.28 (0.11)
SN8	2.38 (0.90)	0.87 (0.08)
SN9	2.50 (0.05)	0.78 (0.16)
SN10	3.17 (0.11)	1.48 (0.09)
SN11	2.74 (0.10)	0.97 (0.18)
SN12	2.57 (0.10)	1.96 (0.22)
SN13	2.92 (0.62)	1.31 (0.33)
SN14	3.02 (0.64)	0.95 (0.15)
SN15	0.72 (0.46)	0.21 (0.13)
SN16	1.29 (0.15)	0.55 (0.26)
SN17	2.20 (0.06)	0.87 (0.19)
SN18	2.69 (0.52)	1.26 (0.31)
SN19	0.78 (0.18)	0.41 (0.09)

880
881
882
883
884
885
886
887
888

889 Table 3. Spearman correlation coefficients obtained for each pair of variables. L* = CIELAB
 890 lightness, Cab* = CIELAB chroma, hab° = CIELAB hue, Fe = elemental iron, PM10 = particulate
 891 matter, h_480nm = semi-quantitative data of mixed iron oxide minerals, h_535nm= semi-
 892 quantitative data of hematite.

	L*	Cab*	hab°	Fe	PM10	h_480nm	h_535nm
L*	1.00						
Cab*	0.08	1.00					
hab°	-0.11	-0.90	1.00				
Fe	-0.20	0.85	-0.80	1.00			
PM10	-0.11	0.81	-0.74	0.96	1.00		
h_480nm	-0.47	0.69	-0.60	0.84	0.75	1.00	
h_535nm	-0.28	0.85	-0.83	0.86	0.81	0.81	1.00

893
 894
 895
 896
 897
 898
 899
 900
 901
 902
 903
 904
 905
 906
 907
 908
 909
 910

911 **CRedit author statement**

912

913 **Pietro Morozzi:** Conceptualization, Methodology, Formal analysis, Investigation, Writing - Original
914 Draft, Visualization; **Barbara Ballarin:** Resources, Writing - Review & Editing; **Erika Brattich:**
915 Writing - Review & Editing; **Franco Lucarelli:** Validation, Resources, Writing - Review & Editing;
916 **Silvia Nava:** Validation, Resources, Writing - Review & Editing; **Pedro J. Gómez-Cascales:**
917 Investigation; **Jose A. G. Orza:** Software, Formal analysis, Resources, Writing - Review & Editing,
918 Supervision, Project administration, Funding acquisition; **Laura Tositti:** Conceptualization, Writing
919 - Review & Editing, Supervision

920

921 **Declaration of interests**

922

923 ☒ The authors declare that they have no known competing financial interests or personal
924 relationships that could have appeared to influence the work reported in this paper.

925

926 ☐The authors declare the following financial interests/personal relationships which may be considered as
927 potential competing interests:
928

929